

## Subtropical-polar jet interactions in Southern Plains dust storms

Michael L. Kaplan,<sup>1</sup> Ramesh K. Vellore,<sup>2</sup> John M. Lewis,<sup>1,3</sup> S. Jeffrey Underwood,<sup>4</sup> Patricia M. Pauley,<sup>5</sup> Jonathan E. Martin,<sup>6</sup> Robert M. Rabin,<sup>3,7</sup> and R. Krishnan<sup>2</sup>

Received 9 June 2013; revised 12 November 2013; accepted 13 November 2013; published 5 December 2013.

[1] The origin of two separate Southern High Plains dust storms, which occurred over a 2 day period in February 2007, is traced to an interaction between the subtropical jet (STJ) and the polar jet (PJ). A large-scale thermal wind imbalance resulting from the confluence of these two jets led to a series of mesoscale circulations that ultimately produced the dust storms. Understanding the connectivity between the dust storms with differing geometries is central to the present investigation. The study rests on the interpretation of analyses from upper air and surface observations complemented by imagery from satellites, the 32 km gridded data set from the North American Regional Reanalysis, and a fine-resolution (6 km grid) simulation from the Weather Research and Forecasting model. Principal assertions from the present study are (1) scale interaction is fundamental to the creation of an environment conducive to dust storm development, (2) low to middle tropospheric mass adjustment is the primary response to a large-scale imbalance, (3) the mesoscale mass adjustment is associated with circulations about a highly accelerative jet streak resulting from the merger of the PJ and STJ, (4) the structure of the jet streak resulting from this merger governs the evolution of the geometry of the dust plumes, with plumes that initially had a straight-line orientation developing a semicircular geometry, and (5) it is concluded that improvements in dust storm prediction will depend on an augmentation to the upper air network in concert with a flow-dependent data assimilation strategy.

**Citation:** Kaplan, M. L., R. K. Vellore, J. M. Lewis, S. J. Underwood, P. M. Pauley, J. E. Martin, R. M. Rabin, and R. Krishnan (2013), Subtropical-polar jet interactions in Southern Plains dust storms, *J. Geophys. Res. Atmos.*, 118, 12,893–12,914, doi:10.1002/2013JD020345.

### 1. Introduction

[2] Most studies that investigate the dynamical processes pertinent to dust storm generation rely on *Danielsen's* [1968, 1974] paradigm including *Pauley et al.* [1996], J. E. Martin (A Southern Plains wintertime dust storm associated with a robust upper level front, unpublished manuscript, 2008, [http://marrella.meteor.wisc.edu/Martin\\_2008.pdf](http://marrella.meteor.wisc.edu/Martin_2008.pdf)), and *Schultz*

and *Meisner* [2009]. Quasi-geostrophic (QG) dynamics govern this standard viewpoint where cyclogenesis and tropopause folds are large-scale features that generally accompany the dust storms. Through meticulous analysis on isentropic surfaces, *Danielsen* [1974] tracked the descent of high-momentum air from the lower stratosphere to the top of the planetary boundary layer (PBL). Although unmentioned in his studies [*Danielsen*, 1968, 1974], this large-scale descent is consistent with an indirect transverse circulation about the exit region of a jet streak imbedded in the large-scale flow—an indirect circulation theorized by *Eliassen* [1962] and discussed at length by *Carlson* [2012]. The descending plume of momentum in juxtaposition with a surface-based well-mixed/adiabatic PBL delivers the recipe for dust ablation.

[3] In contrast to the QG viewpoint of *Danielsen*, other investigators of dust storms over the Southern High Plains (SHP; Figure 1) have placed emphasis on smaller-scale/mesoscale processes. Essentially, the studies are indicative of mass adjustments in high Rossby number regimes [e.g., *Zack and Kaplan*, 1987; *Karyampudi et al.*, 1995a, 1995b]. Theoretical work of *Zhang et al.* [2002] and simulations documented in *Kaplan and Karyampudi* [1992a, 1992b] and *Kaplan et al.* [1997, 1998] have given support to the action of these smaller-scale processes. Recent work by *Lewis et al.* [2011] and *Kaplan et al.* [2011] has been focused on

<sup>1</sup>Division of Atmospheric Science, Desert Research Institute, Reno, Nevada, USA.

<sup>2</sup>Center for Climate Change Research, Indian Institute of Tropical Meteorology, Pune, India.

<sup>3</sup>National Severe Storms Laboratory, Norman, Oklahoma, USA.

<sup>4</sup>Department of Geology and Geography, Georgia Southern College, Statesboro, Georgia, USA.

<sup>5</sup>Marine Meteorology Division, Naval Research Laboratory, Monterey, California, USA.

<sup>6</sup>Department of Atmospheric and Oceanic Science, University of Wisconsin-Madison, Madison, Wisconsin, USA.

<sup>7</sup>Space Science and Engineering Center, Madison, Wisconsin, USA.

Corresponding author: M. L. Kaplan, Division of Atmospheric Science, Desert Research Institute, 2215 Raggio Pkwy., Reno, NV 89512, USA. (Mike.Kaplan@dri.edu)

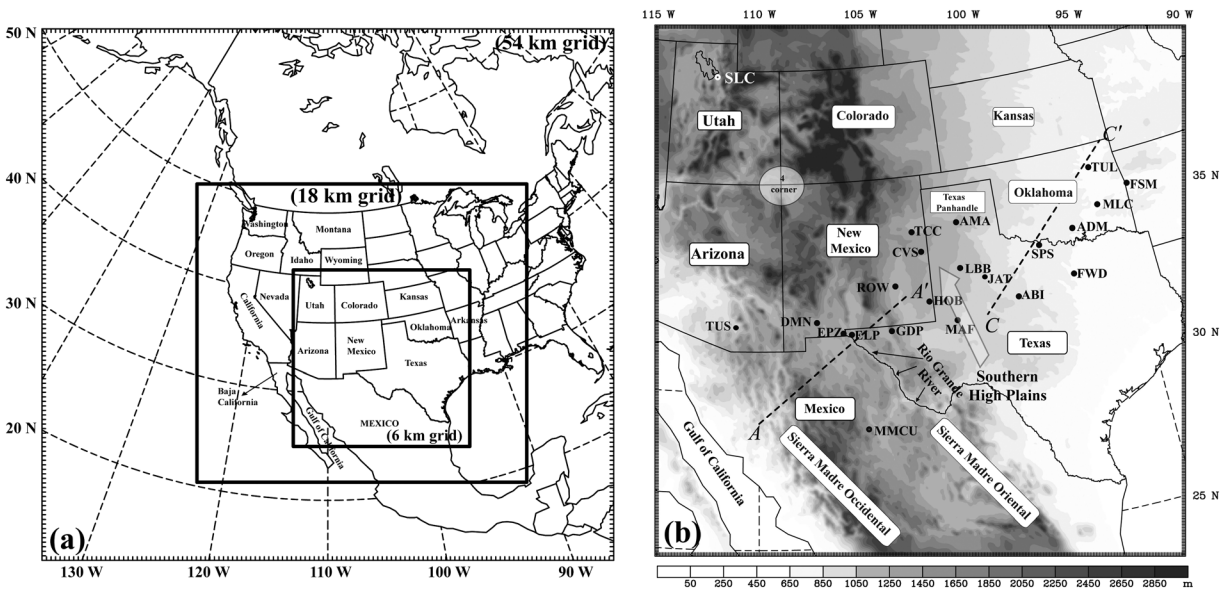


**Figure 1.** (a) WRF modeling domains used in the study and (b) topography (meters) representation in the innermost modeling domain. Overlaid are the cross sections  $A-A'$  and  $C-C'$  (dashed lines), U.S. state identifiers, station locations referenced in the study. The Rio Grande River forms the border between the state of Texas in the U.S. and Mexico. The four corner region is indicated by a circle. The region of Southern High Plains (SHP) is indicated by an arrow.

the role of the mass adjustment mechanism for dust storms that formed over the western United States. Based on evidence from these studies, a reexamination of the Interstate 5 (I-5) dust storm in the San Joaquin Valley of California

in November 1991 indicated that mesoscale processes were important to organize a favorable environment for this event [Kaplan *et al.*, 2013]. Evidence of scale interactions for this dust storm has been supported by the mesoscale Weather

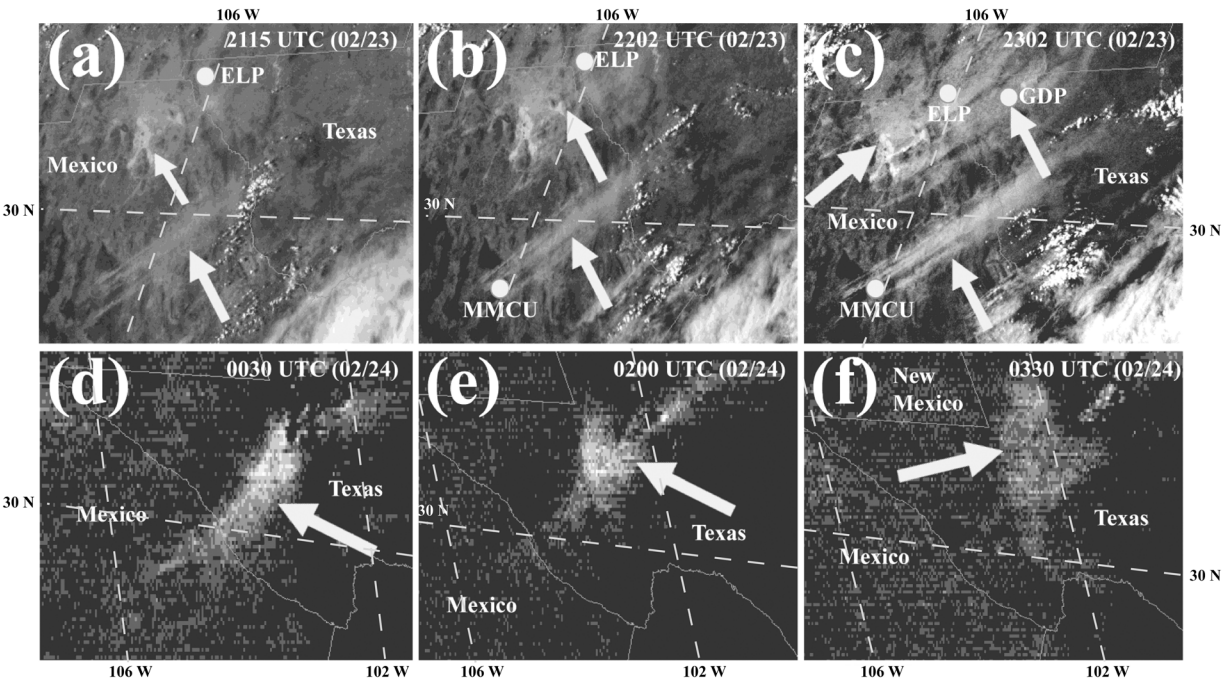


**Figure 2.** Satellite imagery for the DS1 event showing location of dust plumes in the Chihuahua state in Mexico and southwest Texas from 2115 UTC (02/23) to 0330 UTC (02/24). The locations of the stations MMCU, ELP, and GDP are indicated. (a–c) Enhanced visible imagery from GOES 12 (bold arrows indicate the dust storm) and (d–f) the largest values of brightness temperature differences ( $T_b(11.7 \mu\text{m}) - T_b(12.0 \mu\text{m})$ ) from the GOES 11 imager. Elongated and striated bright regions are indicative of dust.

**Table 1.** Maximum Gust Speed ( $\text{m s}^{-1}$ ), and the Lowest Visibility (km) Due to Dust Observed Over Southern High Plains During 23–24 February 2007 (Source: <http://vortex.Plymouth.edu>)

Stations	Maximum Gust Speed ( $\text{m s}^{-1}$ )	Lowest Visibility (km)	Time (UTC)
23 February 2007			
DMN	21	2.5	2100
MMCS	17	1.6	2240
ELP	23	4	2250
GDP	36	9	2350
24 February 2007			
TCC	18	0.3	1320
CVS	24	1.6	1500
HOB	24	4.8	1550
LBB	25	0.3	1600
ABI	21	1.6	1853
SPS	22	1.6	1852
ADM	20	4.1	1955
FWD	24	1.6	2055
MLC	21	3.2	2145
TUL	11	3.3	2210
FSM	18	3.2	2346

Research and Forecasting (WRF) [Skamarock et al., 2008] model simulations. In the spirit of the investigation of the I-5 event, another dust storm previously studied by J. E. Martin (unpublished manuscript, 2008) and Schultz and Meisner [2009]—the 24 February 2007 dust storm in the SHP—is investigated in the present study. This dust storm was categorized as a high impact/severe weather event causing major transportation issues including the closing of Dallas-Fort Worth (FWD) International Airport, Texas, U.S. The previous investigators of this event argued that air parcels rich in kinetic energy were transported into the PBL in association with a prolonged period of sinking. The sinking took place in the polar jet streak’s left entrance region and the descending air parcels were turbulently mixed to the surface and ablated dust. These arguments are in agreement

with the QG processes that govern Danielsen’s paradigm [Danielsen, 1968, 1974].

[4] The present study offers an alternative set of processes that give rise to the dust storms. There is some overlap with the earlier studies [Lewis et al., 2011; Kaplan et al., 2011, 2013] mentioned above. As stated in these earlier studies over the western U.S., there is a mesoscale complement to the QG dynamics, and this is certainly the case for the present study. However, in this 2007 case study, the source of the initial thermal wind imbalance is totally different. The imbalance stems from the merger of the polar jet and the subtropical jet. The juxtaposition of these two strong streams results in a level of geostrophic/thermal wind imbalance far greater and larger than the imbalances discussed in the earlier studies. The mesoscale adjustment to this large-magnitude imbalance displays itself in a variety of ways that differ from the earlier case studies. This should be expected not only from the origin of the imbalance but also from the differing features of the geography in the SHP compared to the Sierra and Coastal Mountains of the West Coast of the U.S. Among these differences is the heat source associated with the Mexican Plateau. Beyond these geographical differences, the study takes on special meaning in the presence of two sequential dust storms that exhibit connectivity.

[5] The possibility of linkage between these two dust storm events is central to the investigation. A battery of products including upper air and surface observations, reanalysis data sets, and numerical model simulations will be brought to bear on the investigation. We begin our study with a synoptic overview and follow up with a discussion of the interplay between the large- and smaller-scale processes that gave rise to this storm.

## 2. Dust Storm Observations

[6] In this section, reference is made to satellite imagery and observations at a series of surface weather stations affected by the dust storm. The geographical locations of these stations along with identifiers are shown in Figure 1. As mentioned earlier, the two dust storms occur less than 1 day apart

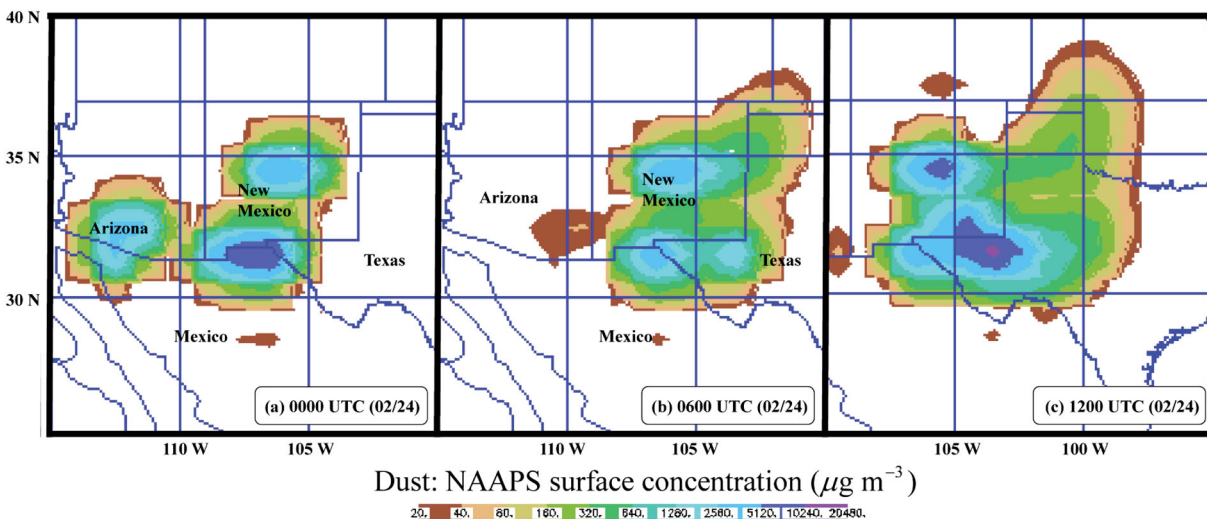


**Figure 3.** Navy Aerosol Analysis and Prediction System (NAAPS) dust concentration simulations ( $\mu\text{g m}^{-3}$ ) at (a) 0000 UTC, (b) 0600 UTC, and (c) 1200 UTC (02/24) (Source: <http://www.nrlmry.navy.mil/aerosol/>).

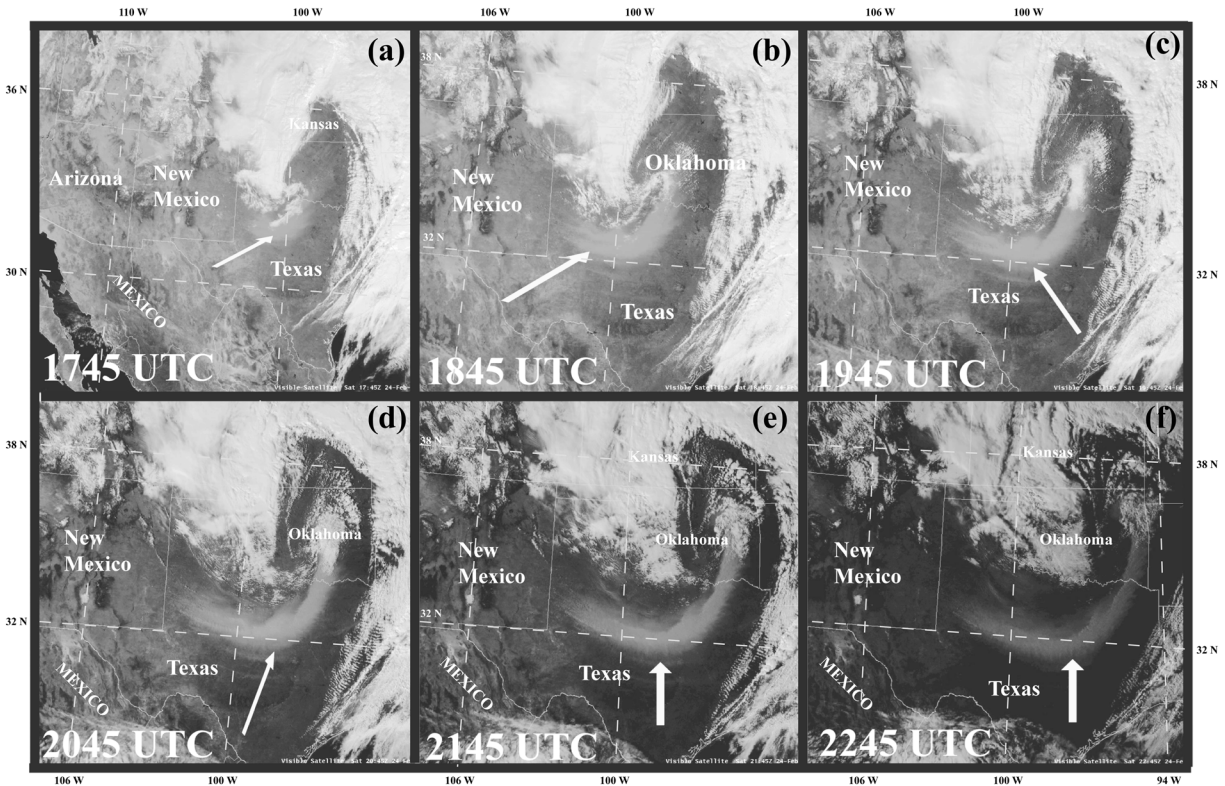


**Figure 4.** GOES 12 visible satellite imagery for the DS2 event valid at (a) 1745 UTC, (b) 1845 UTC, (c) 1945 UTC, (d) 2045 UTC, (e) 2145 UTC, and (f) 2245 UTC (02/24). Bold arrow indicates the dust storm (Source: <http://www.srh.noaa.gov/>). Elongated and striated bright regions are indicative of dust.

—the first during the afternoon and evening of 23 February 2007 (02/23) and the second in the morning through evening of 24 February 2007 (02/24). We simplify reference to these sequential dust storms (DS) with acronyms DS1 and DS2 for storms on 02/23 and 02/24, respectively. A comprehensive discussion of DS2 is found in *Schultz and Meisner* [2009].

### 2.1. Observed Features of DS1

[7] At about 2100 UTC (02/23), visible imagery from Geostationary Operational Environmental Satellite (GOES) 12 indicated the presence of two dust plumes in northeastern Mexico—one approximately 200 km southwest of El Paso, Texas (ELP), U.S., and another further south near Chihuahua (MMCU), Mexico. Visible images of these plumes between 2115 UTC and 2302 UTC (02/23) are shown in Figures 2a–2c. After nightfall, brightness temperature differences are used to depict the movement and extent of the dust plumes (Figures 2d–2f). The brightness temperature differences ( $T_b(11.7\ \mu\text{m}) - T_b(12.0\ \mu\text{m})$ ) were derived from the GOES 11 imagery as employed in *Zhao et al.* [2010] and *Steenburgh et al.* [2012]. Although these infrared images are unable to resolve details of plume geometry, it is apparent that the plumes move into west central Texas 6 h after the dust plumes were initiated.

[8] While most stations in southeastern New Mexico and southwestern Texas (stations south of ELP and Guadalupe Pass (GDP); see Figure 1 for geographical locations) showed surface pressure falls and subsequent gusty winds during the period 2100 UTC (02/23) - 0000 UTC (02/24), only

Deming (DMN) in New Mexico observed low visibility due to dust or haze before 0000 UTC (02/24) (see Table 1, top). However, reduced visibilities accompanying haze were found in surface observations (not shown) between northeastern New Mexico and southwestern Kansas during the period 0000 UTC - 1500 UTC (02/24). It thus becomes problematical to verify the precise location of dust from DS1 after nightfall. More importantly, it is challenging to identify that point in time when DS1 ends.

[9] In an answer to these questions, an aerosol/dust product is examined—the Navy Aerosol Analysis and Prediction System (NAAPS) [*Westphal, 1999; Johnson, 2006*], a modeling tool used for the global aerosol forecasting by the U.S. Navy. The dust concentrations from this product over the time interval 0000 UTC (02/24) - 1200 UTC (02/24) are shown in Figure 3. Here we note the extreme value of dust concentration just southwest of ELP at 0000 UTC (02/24) is consistent in location with the visible imagery shown in Figure 2c. The NAAPS product gives a better impression that the dust is more uniformly spread over the area than seen in the satellite imagery. It leads one to believe that the NAAPS product is more likely to measure the vertically integrated dust concentration as opposed to a surface concentration. Yet, the implied movement of dust into the west Texas area by 0600 UTC (02/24) is consistent with the infrared imagery from satellite shown in Figures 2d–2f. The NAAPS product at 1200 UTC (02/24) indicates a concentration center between Hobbs (HOB), New Mexico, and GDP with an extension into western Kansas. Visible satellite imagery the next morning (1300 UTC (02/24)) gave no sign of dust in this

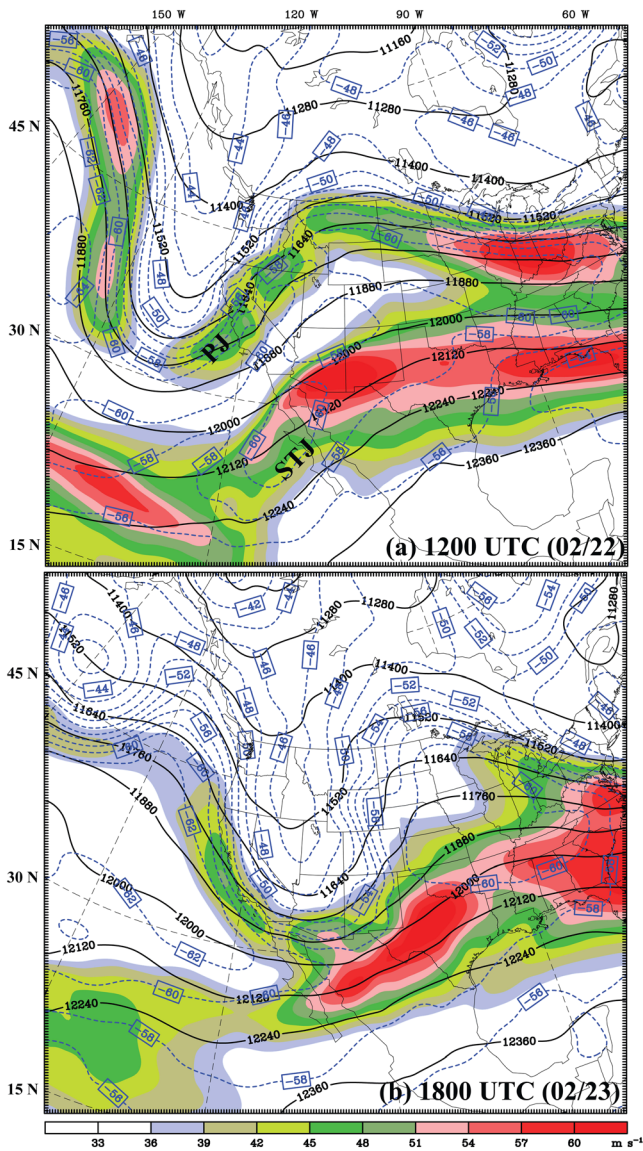


**Figure 5.** 200 hPa horizontal winds (shaded; isotachs;  $\text{m s}^{-1}$ ), geopotential height (solid black lines; contour interval = 120 m), and temperature (dashed blue lines; contour interval = 2°C) from NARR at (a) 1200 UTC (02/22) and (b) 1800 UTC (02/23). PJ = polar jet stream and STJ = subtropical jet stream.

area. Speculation on these unresolved issues will be revisited in section 5 of this paper.

**2.2. Observed Features of DS2**

[10] DS2 commenced during 1400–1500 UTC (02/24), approximately 18 h after DS1 was initiated. It formed in an area between HOB and Lubbock (LBB), Texas. By 1745 UTC (02/24), the dust plume assumed a crescent-shaped form that wrapped from the New Mexico-Texas (see Figure 1 for state identifiers) border in the Texas Panhandle to the midpoint of Oklahoma’s southern boundary (Figure 4). While expanding in breadth along its curved shape, the plume took on a comma-shaped form by 1845 UTC (02/24) that eventually became more semicircular. During the 2000–2200 UTC

(02/24) period, many of the surface weather stations in north central and northeast Texas reported visibilities less than 4 km and wind speeds exceeding  $20 \text{ m s}^{-1}$  (Table 1).

**3. Synoptic-Meso- $\alpha$  Scale Features**

[11] Although we focus on the meso- $\beta$  scale dust storms over the SHP, the larger-scale synoptic-meso- $\alpha$  scale structures in the troposphere are pivotal to the dynamic processes that influence these storms. In this section, we rely on the North American Regional Reanalysis (NARR) [Mesinger *et al.*, 2006] products to discuss these synoptic/meso- $\alpha$  scale features.

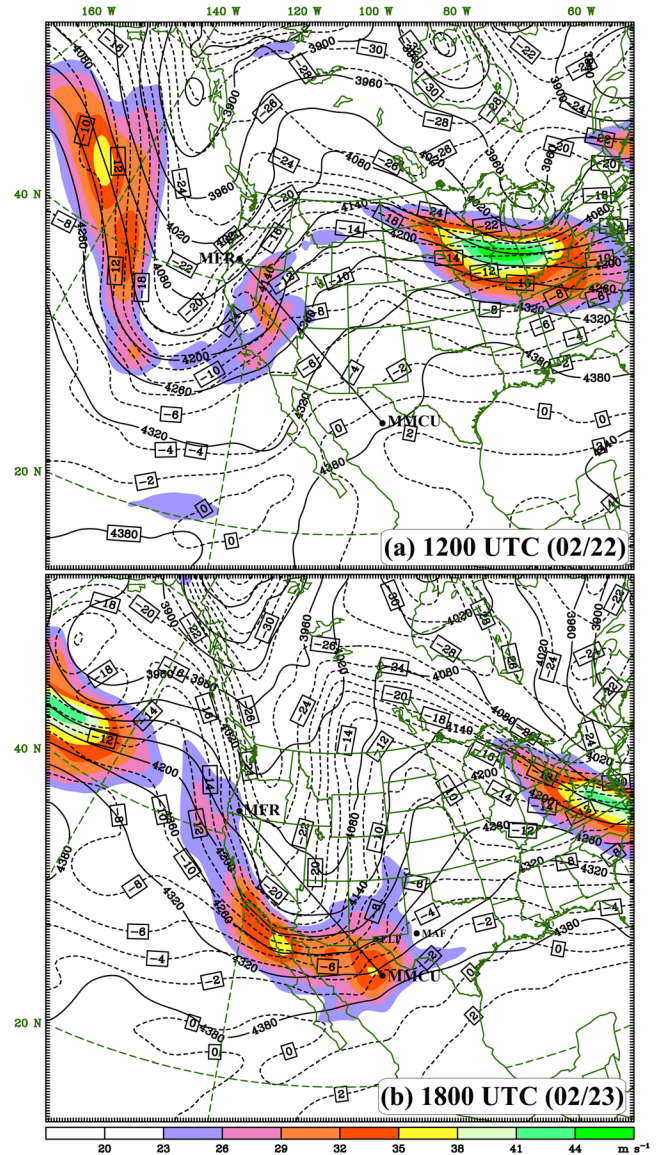


**Figure 6.** 600 hPa winds (shaded; isotachs;  $\text{m s}^{-1}$ ), geopotential height (solid; contour interval = 60 m) and temperature (dashed; contour interval = 2°C) from NARR at (a) 1200 UTC (02/22) and (b) 1800 UTC (02/23). Locations of Medford, Oregon (MFR), MMCu, ELP, and MAF are shown in the figure. A cross section along the line between MFR and MMCu shown here is used in Figure 7.

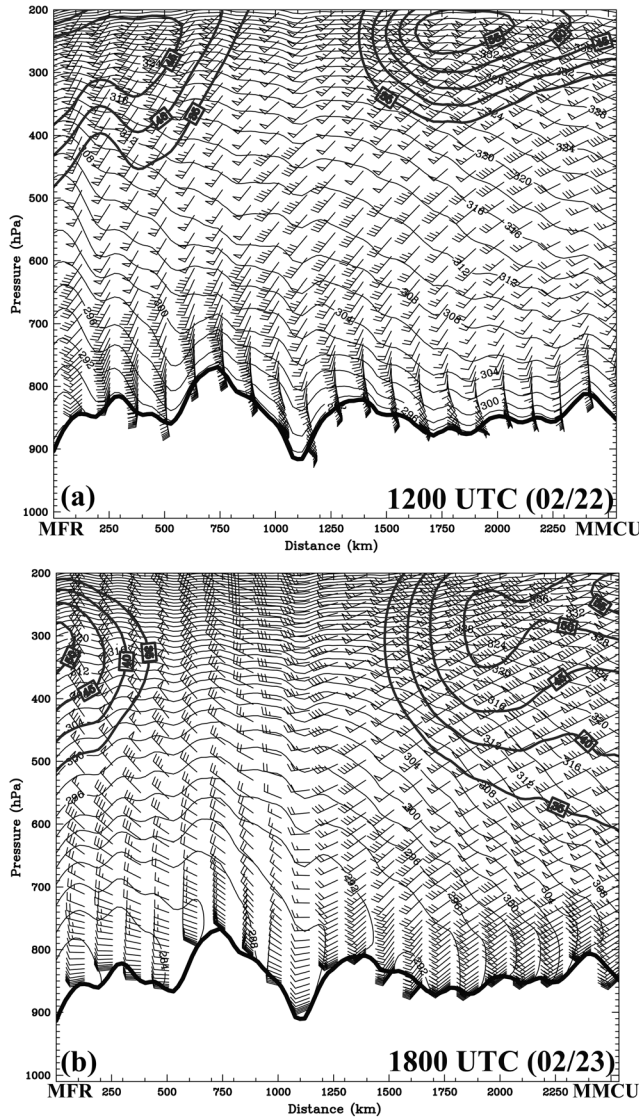


**Figure 7.** Vertical cross section of isentropes (solid contours; contour interval = 2 K), horizontal winds (wind barb =  $5 \text{ m s}^{-1}$ ; isotach intervals at  $5 \text{ m s}^{-1}$  from  $35 \text{ m s}^{-1}$  are indicated by darker contour lines) from MFR to MMCU (see Figure 6) valid at (a) 1200 UTC (02/22) and (b) 1800 UTC (02/23) from NARR.

### 3.1. Confluence of the Jet Streams

[12] Figures 5 and 6 show the 200 and 600 hPa large-scale winds, geopotential height, and temperature fields at 1200 UTC (02/22) and 1800 UTC (02/23), respectively. Most notable features are the two distinct middle tropospheric temperature gradients, one associated with the high-amplitude Rossby wave in the polar jet stream (PJ) and the other associated with the subtropical jet stream (STJ) over northern Mexico. The PJ temperature gradient is somewhat stronger and deeper than the STJ feature. Figure 7 shows the vertical cross section between Medford (MFR), Oregon, and MMCU that bisects these two jets at these times. At 1200 UTC (02/22), a jet core associated with the STJ is located near the southern borders of Arizona and New Mexico and northern Mexico, while the core associated with the PJ is located in the

central California northeastern Oregon region (see Figure 7a, the dual jet cores). The 600 hPa temperature gradients at 1200 UTC (02/22) are distinctly separate with the  $-20^\circ\text{C}$  isotherm to the west of central California and the  $2^\circ\text{C}$  isotherm just southeast of MMCU (Figure 6a). The pressure level 600 hPa was selected for analyses because in previous studies [e.g., Lewis et al., 2011; Kaplan et al., 2011, 2013], highly ageostrophic flow was evident just below this pressure level in the formative stages of dust storms.

[13] A confluence of the two temperature gradient zones and jets takes place over the southwestern U.S. and northern Mexico by 1800 UTC (02/23). The vertical extent of the merger is evident at 200 and 600 hPa (Figures 5b, 6b, and 7b). By this time, the strongest temperature gradient and a unified jet maximum are seen between MMCU and Tucson, Arizona, i.e., about 500 km northwest of MMCU as seen in Figure 7b. The merger process unites these temperature gradients to produce a temperature difference greater than  $20^\circ\text{C}$  extending from central Mexico to the Southern California southwestern Arizona border region. Over the next 6 h, these two jet streaks are united into one middle-upper tropospheric streak over northeastern Mexico and this is consistent with

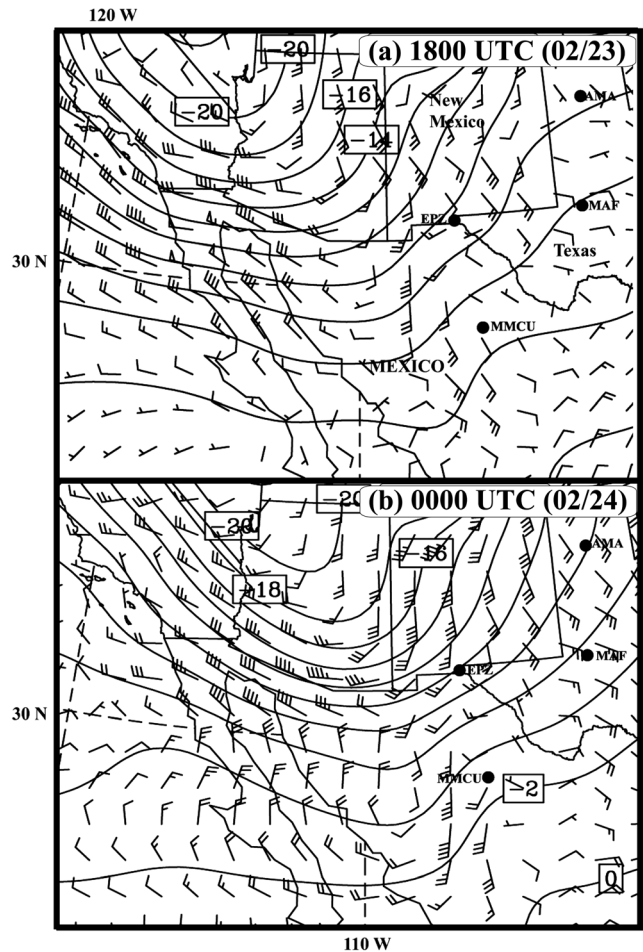


**Figure 8.** Geostrophic wind shear minus true wind shear in the 500–700 hPa layer (full barb =  $5 \text{ m s}^{-1}$ ) diagnosed from NARR valid at (a) 1800 UTC (02/23) and (b) 0000 UTC (02/24). Also shown is the 500–700 hPa layer mean temperature (contour interval =  $2^\circ\text{C}$ ).

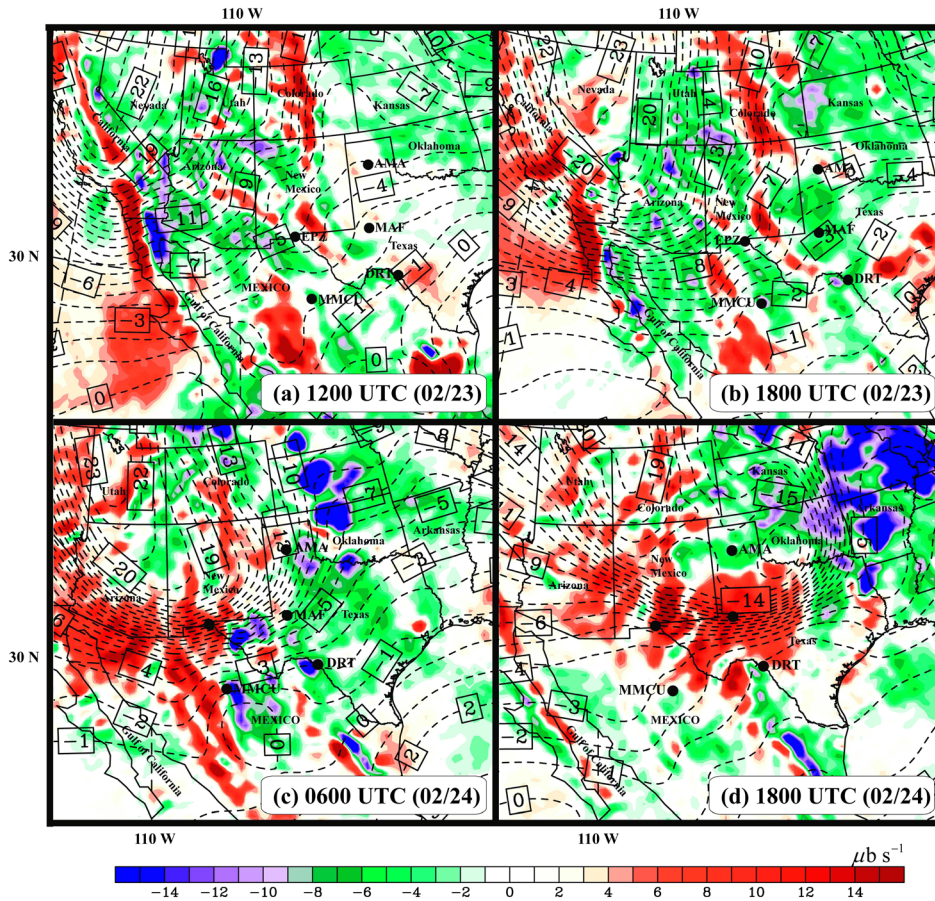


**Figure 9.** Six hundred hectopascal vertical motion (shaded;  $\mu\text{b s}^{-1}$ ) and air temperature (dashed; contour interval =  $1^\circ\text{C}$ ) from NARR at (a) 1200 UTC, (b) 1800 UTC (02/23), (c) 0600 UTC (02/24), and (d) 1800 UTC (02/24). Figures 9c and 9d are shifted to the west.

the confluence of the two temperature gradients by 1800 UTC (02/23) (Figures 5b and 6b). Following this time, the newly formed streak intensifies substantially and becomes progressively more curved as it first exhibits cross-jet and subsequently along-jet ageostrophic flow.

**3.2. Thermal Wind Imbalance**

[14] When the PJ and STJ merge, there is evidence of significant thermal wind imbalance. This is especially noticeable in the 700–500 hPa layer at 1800 UTC (02/23) as shown in Figure 8a. Here we have plotted the vector field,  $\vec{V}_T - \Delta\vec{V}$  where  $\vec{V}_T = \vec{V}_{\text{geos}}^{500\text{hPa}} - \vec{V}_{\text{geos}}^{700\text{hPa}}$  is the geostrophic wind shear (the thermal wind) in the layer and the difference vector  $\Delta\vec{V} = \vec{V}_{\text{obs}}^{500\text{hPa}} - \vec{V}_{\text{obs}}^{700\text{hPa}}$  is the observed wind shear in the layer. The geostrophic wind is denoted by  $\vec{V}_{\text{geos}}$  and  $(\vec{V}_T - \Delta\vec{V})$  is the vector that must be added to the observed wind shear to achieve thermal wind balance. As can be seen in Figure 8, this difference vector exhibits a cyclonic turning with westerlies over Arizona and northwest Mexico, south southeasterly flow over New Mexico, southerly flow over north central Mexico, and southeasterly flow over Texas and Oklahoma.

[15] A recovery of thermal wind balance on the meso- $\alpha$  scale will require a relative cooling of the layer to the west

and northwest of the region that includes southern New Mexico-northern Mexico-southwest Texas, i.e., cooling to reduce the geopotential heights to the west and northwest, thus consistently reducing the veering (anticyclonic) thermal wind relative to the backing and subgeostrophic total wind shear bridging the meso- $\alpha$  and meso- $\beta$  scales of motion. In performing this analysis, it is acknowledged that increasing curvature in time forces the reference state of balance toward gradient wind balance as especially noted in the case studied by Lewis *et al.* [2011]. In short, the thermal balance is achieved by the generalized thermal wind law [Forsythe, 1945].

**Table 2.** Observed 700–500 hPa Layer Mean Temperature ( $^\circ\text{C}$ ) During 23–25 February 2007 From the Rawinsonde Soundings at Santa Teresa (EPZ), Midland (MAF), Amarillo (AMA), and Dallas Fort-Worth (FWD) (Source: <http://Weather.Uwyo.edu>)

	02/23	02/24	02/24	02/25
Stations	1200 UTC	0000 UTC	1200 UTC	0000 UTC
EPZ	-6.9	-10.1	-15.1	-8.0
MAF	-2.5	-5.0	-11.2	-9.1
AMA	-5.0	-8.5	-16.8	-14.5
FWD	-3.8	-3.0	-5.2	-11.2

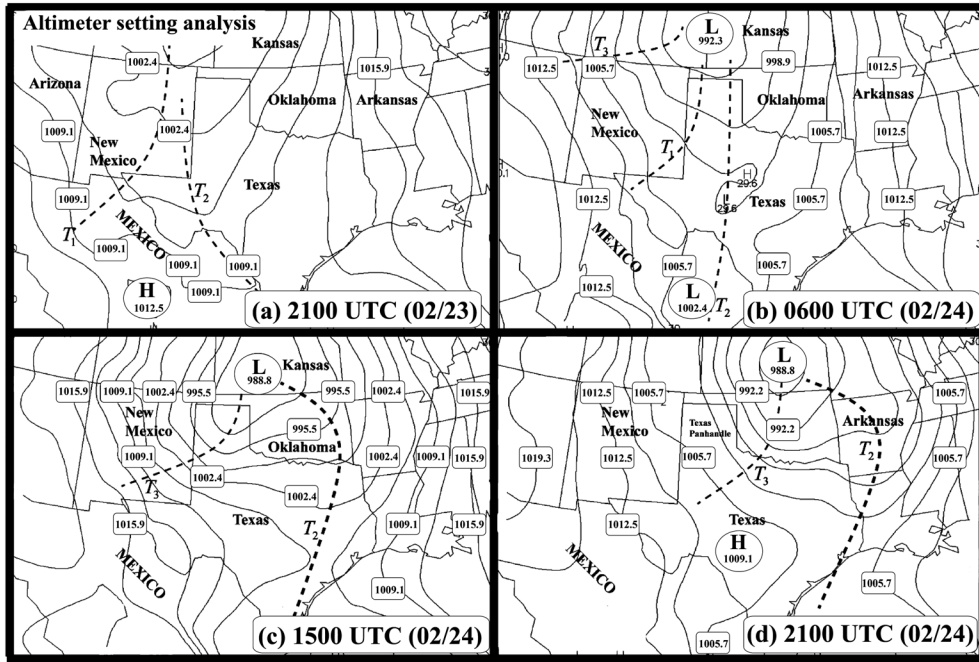


**Figure 10.** Altimeter setting analysis in the Southern Plains (units of inches in Hg; converted to hPa shown inside the boxes) at (a) 2100 UTC (02/23), (b) 0600 UTC (02/24), (c) 1500 UTC (02/24), and (d) 2100 UTC (02/24) (Source: <http://vortex.plymouth.edu>). Also indicated are the surface troughs  $T_1$ ,  $T_2$ , and  $T_3$  referenced in the study.

[16] Evidence of lower-middle tropospheric cooling is shown in Figure 9, a display of the geopotential height, temperature, and Lagrangian derivative of air pressure ( $\omega$ ) at the 600 hPa level. A single cold pool over Nevada at the earliest time divides into two cold pools at the latest time—one that moves from central Nevada to the four-corner area (indicated in Figure 1, circular region) and another that appears over northwest Texas and southwestern Oklahoma. This cold pool over the Texas-Oklahoma area is interpreted as a change on this meso- $\beta/\alpha$  scale that occurs primarily during the 0000–0900 UTC (02/24) time period. Also note the band of ascent (and inferred adiabatic cooling) that moves from the line connecting the stations ELP-MMCU at 1800 UTC (02/23) (Figure 9b) into the region from northeastern Mexico/south of the Texas Panhandle (Figure 1) at 0600 UTC (02/24) (Figure 9c) and finally into southwestern Oklahoma by 1800 UTC (02/24) (Figure 9d). This occurs in the presence of the newly merged jet streak that intensifies and becomes progressively more curved. Thus, the lifting and adiabatic cooling moves from southwest to northeast over this period and is a major contributor to the cooling over the region from northeastern Mexico to well south of the Texas Panhandle and southwestern Oklahoma. This cooling occurs on the right front flank and ahead of the newly formed 600 hPa wind maximum shown in Figure 6. This cooling is also confirmed from rawinsonde observations at Santa Teresa (EPZ), New Mexico, Midland (MAF), and Amarillo (AMA), Texas, during 0000 UTC (02/23) - 0000 UTC (02/24) and at FWD from 0000 to 1200 UTC (02/24) (see also Table 2 and Figure 13). Further explanation and discussion of these features are found

in the next section that makes use of WRF simulations on smaller scales than can be captured by NARR.

### 3.3. Meso- $\alpha$ Scale Surface Features

[17] The lower tropospheric cooling discussed above occurred in conjunction with noticeable pressure structures/perturbations at the surface (Figures 10 and 11). The development and movement of three pressure troughs (denoted by  $T_1$ ,  $T_2$ , and  $T_3$ ) are key features in these surface patterns. Prior to development of DS1, i.e., at 1500 UTC (02/23), a northeast-southwest-oriented pressure perturbation (shown in Figure 10a, denoted by  $T_1$ ) extends from southeastern New Mexico to northeastern Mexico. The anticyclonic inflection in the pressure field as well as the leading cyclonic perturbation accompanying  $T_1$  are both encompassed by a substantial northeast-southwest-oriented mean sea level pressure ( $P_{MSL}$ ) fall corridor during the 1500–2100 UTC (02/23) time period. The descriptor of  $T_1$  as a “trough” (Figures 10a and 11a) is based on these strong and persistent pressure falls. This trough is nearly coincident with the location of the jet streak merger as well as the development and subsequent expansion of DS1 during the period 2100 UTC (02/23) - 0300 UTC (02/24).  $T_1$  deepens and builds poleward to merge with the intensifying synoptic-scale cyclone over western Kansas by 0600 UTC (02/24) (Figure 10b).

[18] A newly developed surface trough  $T_2$  is seen over west Texas at 0600 UTC (02/24) (Figure 10b). It separates from  $T_1$  accompanying a rapid pressure jump over west Texas which decouples  $T_1$  from  $T_2$ . This trough ( $T_2$ ) weakens in time as it moves across Texas triggering convection well east and south

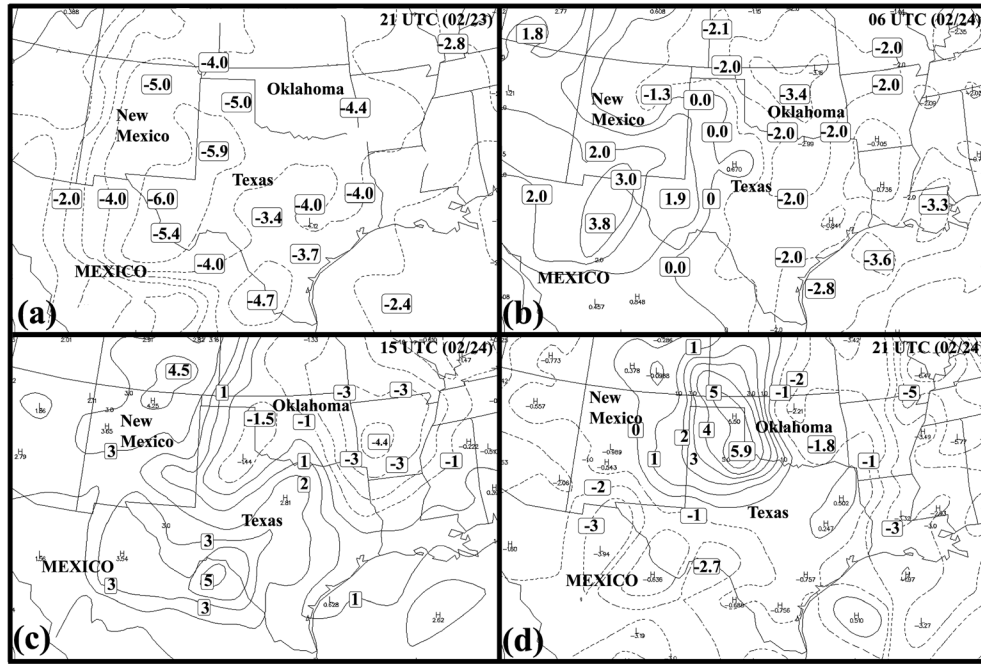


**Figure 11.** Observed 3 h sea level pressure tendency (hPa per 3 h; solid = positive; dashed = negative values) in the Southern Plains at (a) 2100 UTC (02/23), (b) 0600 UTC (02/24), (c) 1500 UTC (02/24), and (d) 2100 UTC (02/24) (Source: <http://vortex.plymouth.edu>).

of DS2 but is followed by the intensification of another surface trough  $T_3$  by 1500 UTC (02/24) in and south of the Texas Panhandle area (Figure 10c).  $T_3$  rotates equatorward of the extratropical cyclone in Kansas to be colocated with the downstream propagation of DS2 just before 2100 UTC (02/24) (Figure 10d).

[19] Observed  $P_{\text{MSL}}$  tendencies (Figures 11a–11d) indicate regions of pressure falls followed by rises that move from northeastern Mexico to west and central Texas over the period of DS1 and DS2 development, i.e., from late on 23 February (02/23) to late on 24 February (02/24). Strong pressure falls occur with  $T_1$  during 1500 UTC (02/23) to 0000 UTC (02/24) over the New Mexico–Texas border. These  $P_{\text{MSL}}$  falls redevelop and move into central Texas during 0300 UTC (02/24) to 0900 UTC (02/24) with the formation of  $T_2$ . This is followed by the  $P_{\text{MSL}}$  falls over the Texas Panhandle after 1200 UTC (02/24) that spread into north central Texas by 1500 UTC (02/24) with the formation of  $T_3$ .

[20] The regions of  $P_{\text{MSL}}$  falls that accompany the development of  $T_1$ ,  $T_2$ , and  $T_3$  and followed by  $P_{\text{MSL}}$  rises in Figure 11 closely track the middle-upper tropospheric divergence, ascent, and cooling in response to thermal wind imbalance in association with the newly merged jet streak described earlier. Furthermore, the  $P_{\text{MSL}}$  falls during the period spanning 1500 UTC (02/23) to 0900 UTC (02/24) over west Texas are as strong as the pressure falls associated with the large-scale cyclone over northwestern Kansas, and this is consistent with the swath of 600 hPa cooling in response to the ascent accompanying the falls, shown in Figure 9, well south of the cyclone. The  $P_{\text{MSL}}$  falls follow the motion of the 600 hPa wind maximum analogous to the 600 hPa cooling (Figures 6 and 9). The details of these adjustments demand data sets much finer

than NARR and radiosondes which will be discussed in the next section.

#### 4. Mesoscale Signatures From the WRF Simulation

[21] The analyses based on NARR and surface data examination indicated linkages between the dust events in the region between northeastern Mexico and north central Texas during the 1500 UTC (02/23) to 1500 UTC (02/24) time period. In this section, an effort is made to view and discuss DS1 and DS2 from an encompassing mesoscale perspective. That is, as opposed to viewing these dust events separately, we follow a continuous stream of mesoscale processes that govern the life cycle of these dust storms. These processes are fundamentally linked to the evolving jet streak that formed after the STJ and PJ merger. The dust serves as a tracer of disturbances that generate low-level turbulence kinetic energy (TKE) in the flow regime, but paramount to the study is a description of mesoscale processes that form in response to dynamic imbalance with this jet streak.

##### 4.1. WRF Model Setup and Verification

[22] The mass core version of the WRF model (version 3.4) used in this study employs three domains. The domains are shown in Figure 1a. The horizontal grid spacing for these domains is 54, 18, and 6 km. The model configuration has 71 levels in the vertical and the interactive strategy between the domains is one way. The model physics configuration includes (i) an Eta surface layer scheme [Janjić, 2001], (ii) the Mellor–Yamada–Janjić 1.5 order (level 2.5) turbulence closure model [Mellor and Yamada, 1974, 1982; Janjić,

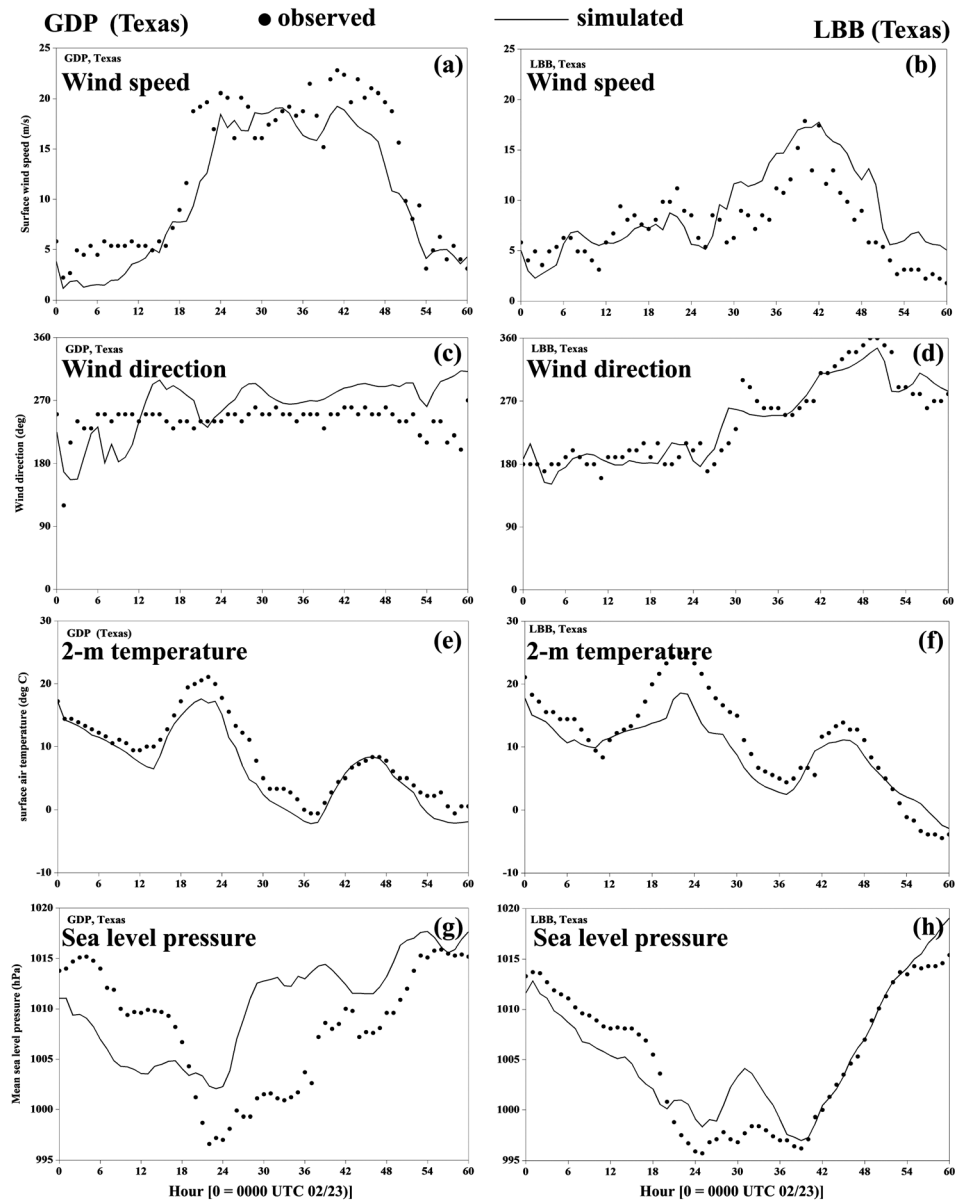


**Figure 12.** Observed (black circles) and WRF (6 km grid) simulated (solid line) hourly time series of (a, b) surface (10 m) wind speed ( $\text{m s}^{-1}$ ) and (c, d) wind direction (deg), (e, f) surface (2 m) air temperature ( $^{\circ}\text{C}$ ), and (g, h) sea level pressure (hPa) during 0000 UTC (02/23) to 1200 UTC (02/25) at GDP (left column) and LBB (right column) (x axis represents time; 0 = 0000 UTC (02/23); 60 = 1200 UTC (02/25)).

2001], (iii) the Betts-Miller-Janjić cumulus scheme [Betts, 1986; Betts and Miller, 1986; Janjić, 1994], applied only on the 54 and 18 km grids, (iv) Morrison’s double-moment cloud microphysical scheme [Morrison *et al.*, 2009], (v) the Rapid Radiative Transfer Model for long-wave radiation [Mlawer *et al.*, 1997] as well as Dudhia’s short-wave radiation scheme [Dudhia, 1989], and (vi) the Noah land surface model [Chen and Dudhia, 2001; Ek *et al.*, 2003]. This configuration of parameterization schemes resulted in physically realistic simulations in the two previously cited studies [Kaplan *et al.*, 2011, 2013] on dust storms over arid elevated terrain in which there was virtually no moist convection.

[23] Initialization and boundary value specification is accomplished by recourse to products from the National Center for Environmental Prediction’s (NCEP’s) global forecast model

(the Global Forecast System (GFS); <http://rda.ucar.edu/datasets/ds083.2>) [Kalnay *et al.*, 1990]. The WRF was initialized at 0000 UTC (02/23) i.e., 21 h prior to the onset of DS1. The GFS analysis ( $1^{\circ} \times 1^{\circ}$  resolution) was found to be superior to NARR (32 km grid) for this case study at this time. The NARR initialized simulation led to excessive deepening of the Rossby wave as the system moved over the southwestern U.S. and northern Mexico. There were obvious errors in the NARR height and wind fields at key locations in southern Arizona and north central Mexico at this time—errors detailed through comparison with rawinsonde observations in that area. At other times, NARR and GFS were in much closer agreement.

[24] WRF simulations are compared with surface and upper air observations as shown in Figures 12 and 13, respectively.

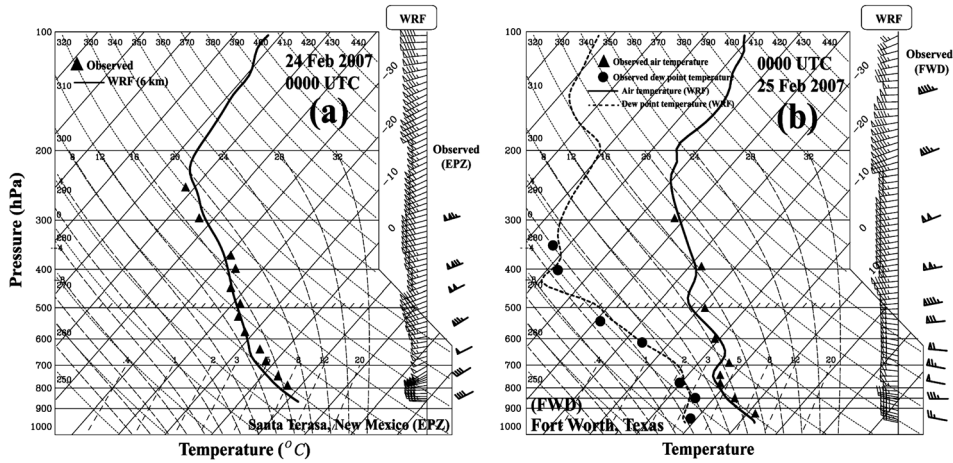


**Figure 13.** Observed (triangles and circles) and WRF (6 km grid) simulated (solid and dashed lines) sounding at (a) EPZ at 0000 UTC (02/24) and at (b) FWD, Texas, at 0000 UTC (02/25) (see Figure 1 for the station locations).

One notes a close correspondence between the simulated and observed surface features in the  $P_{MSL}$ , wind, and temperature fields at GDP and LBB—stations close to the location of the strongest signals associated with DS1 and DS2. The WRF-simulated pressure trace at GDP captures the precipitous fall and subsequent rise in pressure over the 60 h period shown, but the amplitude of this trace is only half of the observed amplitude, and the timing of the most significant pressure fall is early. It is speculated that this amplitude error reflects a mismatch between the location of the model’s grid points on the 6 km grid and the location of the observation site at GDP. Essentially, the hydrostatic builddown to sea level used different elevations, and this led to incompatible values of the  $P_{MSL}$ . In view of the excellent fit between the patterns of WRF-simulated temperature and observed temperature, the amplitude difference in the  $P_{MSL}$  traces is likely less related to differences in air temperature at grid points and observation location and more related to builddown errors. The WRF-simulated thermodynamic structure shown in Figure 13 (and Table 2) is remarkably accurate—especially in respect to the depth of the adiabatic layers at both EPZ and FWD. The observed and simulated hodographs are also in good agreement with each other. As previously noted and as will be shown later, these deep adiabatic layers are commonplace in strong dust storm events.

**4.2. Lagrangian Synthesis of Thermal Wind-Mass Adjustments**

[25] The back trajectories associated with the large-scale synoptic system are displayed in Figure 14. Back trajectory 1 covers a period of 24 h, while back trajectories 2 and 3 cover a 33 h period. The air parcel on trajectory 1 (parcel #1) essentially followed a plan view straight line with minor vertical oscillations between 700 and 900 hPa. This trajectory was governed by the winds in the STJ. Parcel #2’s path was nearly a straight-line plan view along the U.S.-Mexico border

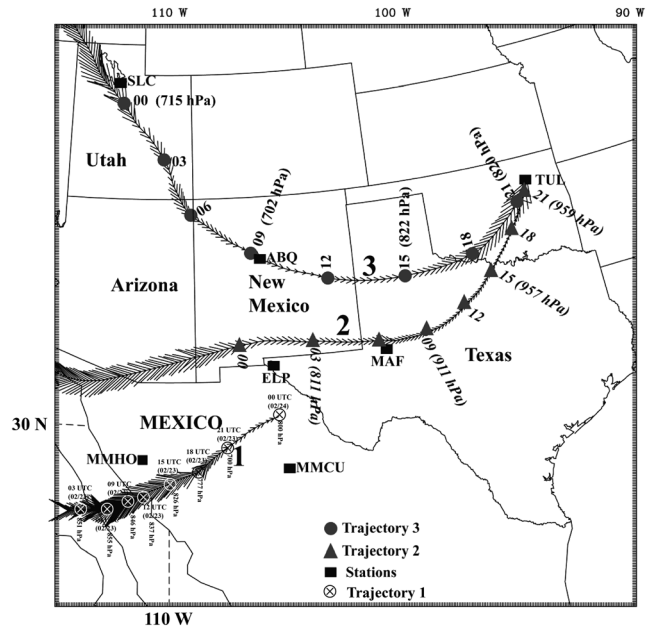


**Figure 14.** Plan view of trajectory analysis from 6 km WRF grid for 24 h back trajectory ending at 800 hPa above 29.25°N, 106.2°W in Mexico at 0000 UTC (02/24)—trajectory 1, and 33 h back trajectory ending at 960 hPa (800 hPa) above Tulsa (TUL), Oklahoma, U.S., at 2200 UTC (02/24)—trajectory 2 (trajectory 3). The 3-hourly position of the parcel (circled times for trajectory 1, solid triangles for trajectory 2, and solid circles for trajectory 3) valid from 0000 UTC 24 February 2007, and the pressure level where it is located are also indicated in the figure. The width of the arrows indicates the rising (wide) and sinking (narrow) of the parcel motion (SLC = Salt Lake City, Utah; ABQ = Albuquerque, New Mexico; MMHO = Hermosillo, Mexico). The back trajectories were calculated using the RIP (Read Interpolation Plot) visualization program [Stoelinga, 2009].

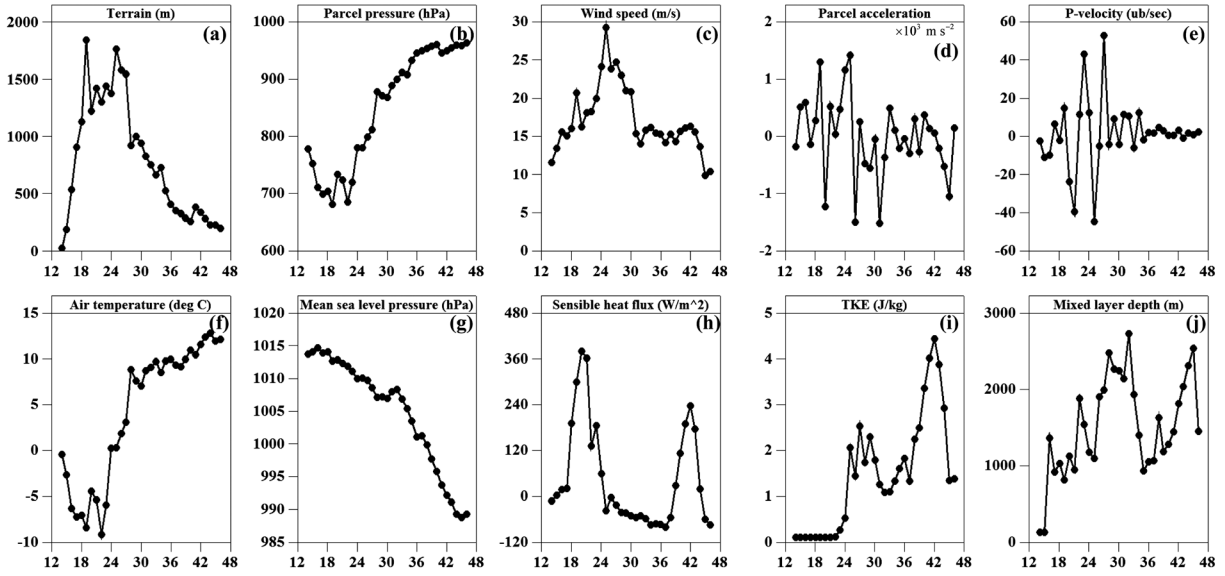


**Figure 15.** Hourly diagnostics (WRF 6 km grid) for parcel trajectory 2 shown in Figure 14. The  $x$  axis indicates time in hours, starting from 1200 UTC (02/23) and ending at 0000 UTC (02/25). Shown in the figure are (a) terrain elevation (m) and (b) the pressure (hPa) at the parcel location, (c) horizontal wind speed ( $\text{m s}^{-1}$ ), (d) parcel acceleration ( $\times 10^3 \text{ m s}^{-2}$ ), (e)  $\omega$  ( $\mu\text{b s}^{-1}$ ), (f) air temperature ( $^{\circ}\text{C}$ ), (g)  $P_{\text{MSL}}$  (hPa), (h) sensible heat flux at the surface ( $\text{W m}^{-2}$ ), (i) TKE ( $\text{J kg}^{-1}$ ), and (j) mixed layer depth (m) along the back trajectory.

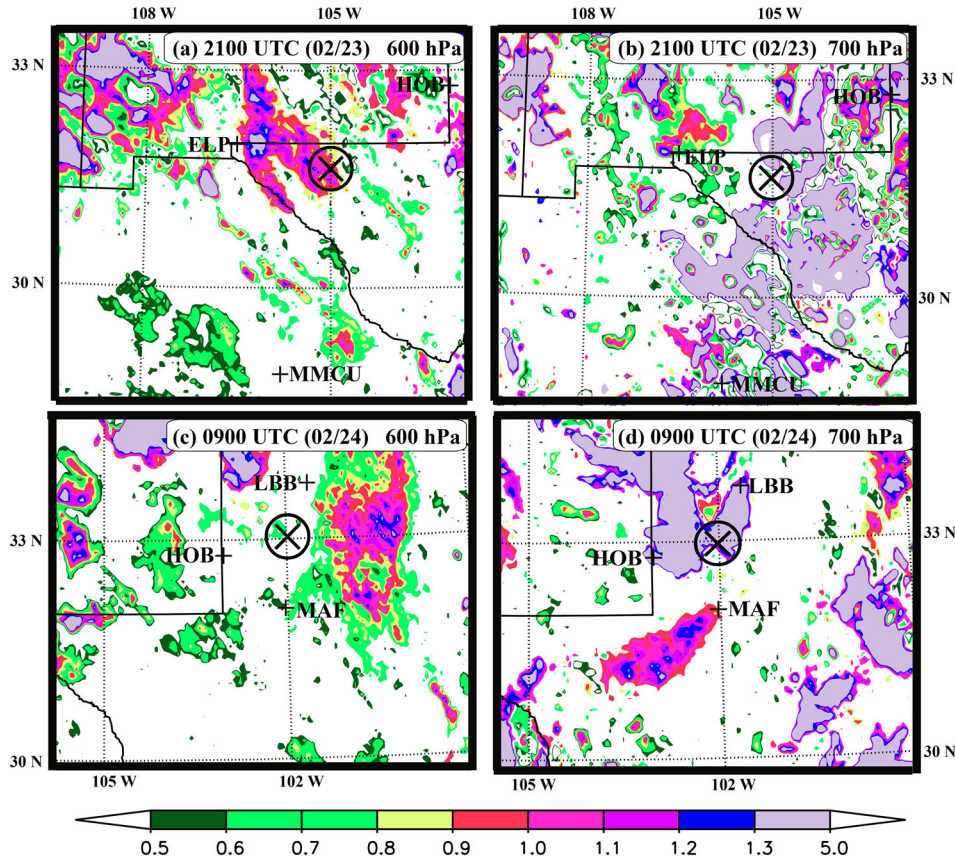


**Figure 16.** WRF (6 km grid) diagnosed Lagrangian Rossby number ( $Ro^L$ ) at 2100 UTC (02/23) on (a) 600 hPa and (b) 700 hPa, and  $Ro^L$  at 0900 UTC (02/24) on (c) 600 hPa and (d) 700 hPa. Circled times indicates the location of the dust plumes from DS1 in Figures 16a and 16b and from DS2 in Figures 16c and 16d. The solid line indicates the state boundaries.

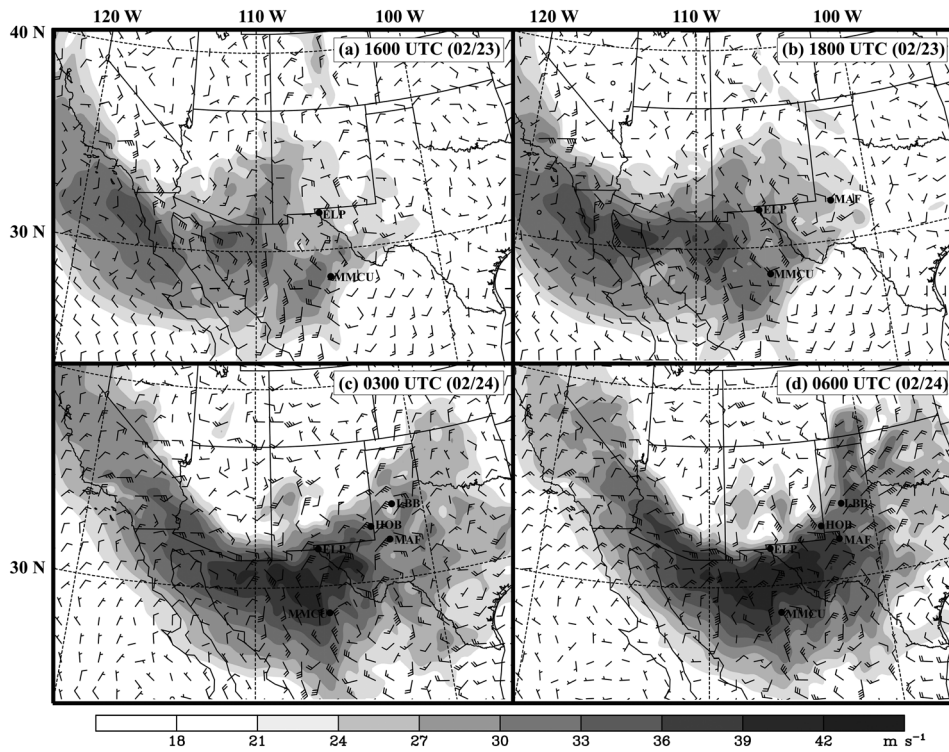


**Figure 17.** 600 hPa ageostrophic wind (full barb =  $5 \text{ m s}^{-1}$ ) and total wind speed (shaded;  $\text{m s}^{-1}$ ) diagnosed from the 18 km simulation valid at (a) 1600 UTC (02/23), (b) 1800 UTC (02/23), (c) 0300 UTC (02/24), and (d) 0600 UTC (02/24).

before it executed an abrupt cyclonic turn and descended another 50 hPa prior to its arrival above Tulsa, Oklahoma (TUL). Parcel #2 was under the influence of the STJ during the first 20–21 h of its movement, but it was clearly under the influence of the combined STJ-PJ during the last 12 h. Parcel #3 had a long cyclonically curved/descending path from Salt Lake City, Utah (SLC), to TUL. From a plan view perspective, this path had similarity to those associated with

the Danielsen paradigm [Danielsen, 1974; Pauley et al., 1996]. But the vertical descent over this long trajectory was only about 100 hPa as opposed to typical descents of 600–800 hPa for cases that were consistent with the Danielsen paradigm associated with the tropopause fold phenomenon [Danielsen, 1974].

[26] Figure 15 displays the temporal traces of physical process (parcel diagnostics) associated with parcel #2. During

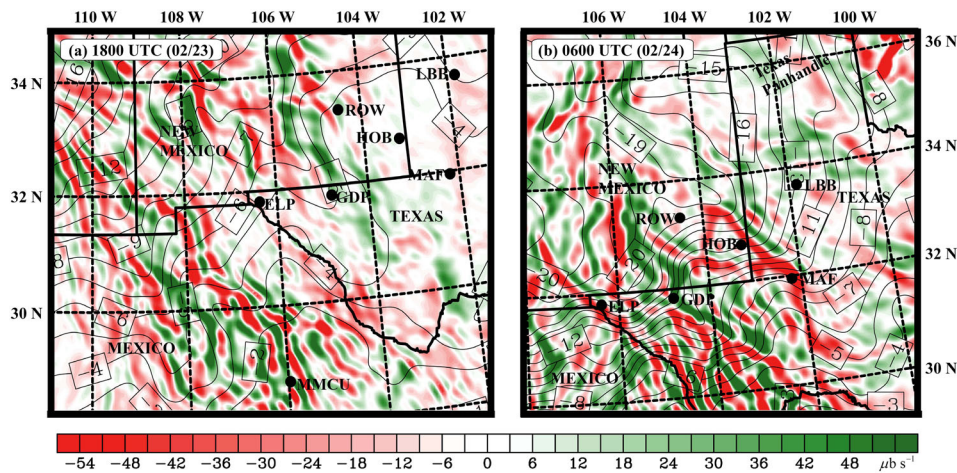


**Figure 18.** WRF (6 km grid) 600 hPa vertical motion (shaded;  $\mu\text{b s}^{-1}$ ) and air temperature (contour interval =  $1^\circ\text{C}$ ) at (a) 1800 UTC (02/23) and (b) 0600 UTC (02/24). Thick lines indicate the U.S. state boundaries and the regions surrounding Texas, New Mexico, U.S., and Mexico are only shown in the figure.

**Table 3.** Terms in Equation (2) Diagnosed at 600 hPa (Columns 5–8  $\times 10^{-8} \text{ s}^{-2}$ ), Mean Sea Level Pressure ( $P_{\text{MSL}}$ ) and Lagrangian Derivative of Air Pressure ( $\omega$ ) at Different Locations (A = 32.5°N, 107.5°W, B = 32.5°N, 102°W, and C = 33.5°N, 98°W) Along the Trajectory 2 (See Figure 14)<sup>a</sup>

Location	Time (UTC)	$P_{\text{MSL}}$ (hPa)	$\omega$ ( $\mu\text{b s}^{-1}$ )	$\frac{dD}{dt}$	$f\zeta - u\beta + 2J(u,v)$	$-\nabla^2\Phi$	$R_\omega$	Vertical Advection ( $\text{K h}^{-1}$ )	Horizontal Advection ( $\text{K h}^{-1}$ )
A	12 (02/23)	1014.5	10.07	4.48	-0.06	-22.81	28.02	2.04	-2.64
	15 (02/23)	1014.2	10.37	-43.52	1.14	-78.23	33.57	0.16	-0.84
	18 (02/23)	1006.5	0.43	-1.17	-5.26	-8.00	12.33	0.12	-2.08
	21 (02/23)	1004.4	-10.78	23.08	1.75	-2.51	24.00	-2.62	8.60
	00 (02/24)	1010.7	-37.52	-14.95	12.50	14.54	-35.74	-10.22	9.02
B	03 (02/24)	1019.4	52.72	-34.30	-0.89	-8.65	-24.69	18.29	-14.81
	21 (02/23)	999.9	-6.05	-5.11	-8.17	10.47	-6.89	-0.78	0.09
	00 (02/24)	1000.3	-14.35	31.06	14.11	-18.19	37.88	-0.58	0.65
	03 (02/24)	1002.8	-34.69	55.35	24.71	22.87	7.92	-1.05	0.45
	06 (02/24)	1007.4	19.24	10.78	9.98	-22.86	25.05	4.51	-8.35
	09 (02/24)	1008.0	-13.65	38.92	5.25	-15.73	49.79	-4.79	2.38
	12 (02/24)	1005.7	30.24	-43.41	-2.47	-40.77	-0.12	7.98	-6.51
C	06 (02/24)	1003.6	22.22	-54.96	-53.67	14.68	1.42	-0.77	-1.59
	09 (02/24)	999.6	32.82	56.76	-3.01	89.62	48.97	11.15	-0.81
	12 (02/24)	1000.2	2.85	11.69	-2.45	-4.56	18.89	0.57	-3.25
	15 (02/24)	998.4	5.87	-49.39	-11.21	-31.93	-6.30	2.05	-4.98
	18 (02/24)	995.0	3.62	7.17	2.04	-9.82	15.56	0.54	1.29
	21 (02/24)	998.1	4.29	-5.21	-1.13	-0.16	-3.38	0.59	0.48

<sup>a</sup>Also shown is the horizontal and vertical advection of potential temperature at 600 hPa (units in  $\text{K h}^{-1}$ ).

the 1800 UTC (02/23) to 0600 UTC (02/24) period, parcel #2 traverses the region of the U.S.-Mexico border while DS1 is occurring. The air parcel is located between 700 and 800 hPa near EPZ at 0000 UTC (02/24). Since midlevel imbalance (approximately 200–250 hPa above the surface) is our focus based on previous dust storm case study analyses, we will describe the adjustments between 500 and 800 hPa. Prior to this period (1200 UTC (02/23) to 0000 UTC 02/24), the parcel ascended from 800 hPa to 700 hPa over southeastern Arizona-southwestern New Mexico and subsequently was followed by a descent to about 900 hPa by 1200 UTC (02/24) over north central Texas. The region primarily from southeastern Arizona to southwestern New Mexico represents the location of active thermal wind adjustment—approximately 200–250 hPa above the ground—particularly within the merged midtropospheric jet streak’s exit region.

[27] In the following subsections, we will employ Lagrangian diagnostics to relate the trajectory motions to (1) growing imbalance in the flow accompanying strong accelerations, (2) substantial rate of change of divergence in the velocity field, and (3) adiabatic cooling on the right flank of the jet’s exit region (unbalanced for a straight jet) encompassing the region from southeastern Arizona to the New Mexico/Texas border. These adjustments and cooling signals are forcing height falls to reduce the thermal wind imbalance albeit also generating a curved flow state as mentioned earlier. These adjustments are coincident in space and time with the development of  $T_1$  and  $T_2$  over this region on Figures 10a and 10b followed by rapid  $P_{\text{MSL}}$  rise. Examination of the aforementioned is discussed in subsequent subsections.

#### 4.2.1. Rossby Number and Upper Level Ageostrophy

[28] Rossby number ( $Ro$ ) is a measure of atmospheric imbalance via the ratio of advective to the Coriolis accelerations. Smaller ratios of Rossby number on the order of 0.1 are representative of QG dynamics and mesoscale circulations are typically associated with  $Ro^L \gg 1$  whose superscript “L” refers to the Lagrangian calculation of this ratio (equation

(1) below) [Zack and Kaplan, 1987; Van Tuyl and Young, 1982; Zhang et al., 2002; Kaplan et al., 2011, 2013].

[29] The quantitative form of  $Ro^L$  is expressed as follows:

$$Ro^L = \frac{\left| \frac{\partial \vec{V}_H}{\partial t} + (\vec{V}_H \cdot \nabla) \vec{V}_H \right|}{f \left| \vec{V}_H \right|} = \frac{\left| \vec{V}_{ag} \right|}{\left| \vec{V}_H \right|} \quad (1)$$

where  $\vec{V}_H$  is the horizontal wind vector,  $\vec{V}_{ag}$  is the ageostrophic wind vector, and  $f$  is the Coriolis parameter. In this form, it is clear that the Rossby number compares the magnitude in the ageostrophic wind relative to the total wind, which is an intuitively valuable way to view the ratio.

[30] Figure 16 shows the evolution of  $Ro^L$  at the 600 and 700 hPa levels over the period of 2100 UTC (02/23) - 0900 UTC (02/24). This display gives evidence of large-magnitude accelerations and ageostrophy over the areas where DS1 was generated (2100 UTC (02/23)) and maintained as well as in the precursor period of DS2 (prior to 1500 UTC (02/24)). This display also indicates that the region of unbalanced mesoscale dynamics coincides with the region of midtropospheric jet streak formation/intensification—in the region, 500 km equatorward of the extratropical cyclone (see Figures 10 and 17). Parcels #2 and #3 shown earlier overlap near LBB (at different times), the area of increasing Rossby numbers at about 0900 UTC (02/24) which is directly above the strengthening  $T_1$  and developing  $T_2$  (see also Figures 10 and 11).

[31] In view of the large-scale thermal wind imbalance in the 700–500 hPa layer as shown in Figure 8, ageostrophic wind and substantial velocity divergence development in this layer is anticipated and indeed apparent at this key period of parcel imbalance and high Rossby number flow regime (Figures 16 and 17). As lower tropospheric air parcels move out from the region over New Mexico-west Texas after initiation of DS1, i.e., during 2100 (02/23) to 0900 UTC (02/24), the total wind at midtropospheric levels accelerates more

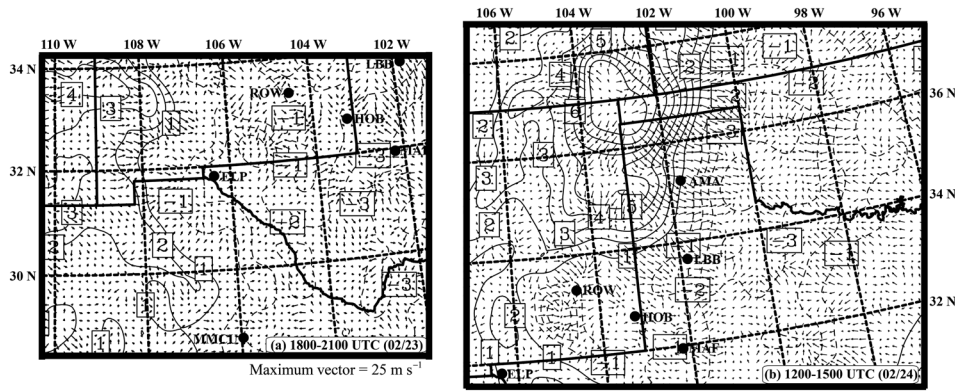


**Figure 19.** WRF (6 km grid) diagnosed isallobaric winds and the 3 h  $P_{MSL}$  tendency (solid (positive)/dashed (negative); contour interval = 1 hPa) during (a) 1800–2100 UTC (02/23) and 1200–1500 UTC (02/24). Regions surrounding Texas, New Mexico, U.S., and Mexico are only shown in the figure. Thick solid line shows U.S. state boundaries.

than  $10 \text{ ms}^{-1}$ , and the ageostrophic wind component is directed leftward and upstream of the midtropospheric jet streak’s exit region between ELP and MAF. This location/time is in proximity to the accelerating high Rossby number regime. It is also a region of ascent followed by descent as the unbalanced motions force the parcel into rising and cooling in the region surrounding the stations ELP-MAF-LBB-HOB followed by sinking and warming east of MAF (Figures 14–17).

**4.2.2. Velocity Divergence and Vertical Motions**

[32] The rising motions dominate the jet exit region from near ELP to MAF in the highly ageostrophic part of the jet exit region during 2100 UTC (02/23) - 0900 UTC (02/24) (Figures 16–18). These rising motions require significant changes in midtropospheric velocity divergence. The equation governing the rate of change of divergence ( $D = \nabla \cdot \vec{V}_H$ ) on the sphere takes the following form:

$$\frac{dD}{dt} = -D^2 + [f\zeta' - u\beta + 2J(u, v)] - \nabla^2\Phi + R_\omega + R_c \quad (2)$$

[33] Terms in equation (2) are defined in Appendix A. The terms are evaluated at the 600 hPa level and shown in Table 3. The most dynamic locations and times of the calculations follow (1) west of ELP during 1800–2100 UTC (02/23) in the early stages of DS1, (2) near MAF during 2100 UTC (02/23) to 0300 UTC (02/24) in the dissipating period of DS1, and (3) at the location downstream from DS2 initiation during 0600 UTC to 1200 UTC (02/24) just northwest of FWD. These locations are also sequentially above  $T_1$  and  $T_2$  as well as downstream from  $T_3$ , respectively (see Figure 10 for the trough locations).

[34] Table 3 and Figure 18a indicate that divergence tendencies following the air motion (equation (2)) create the divergence for ascent and  $P_{MSL}$  falls over north central Mexico and southern New Mexico shortly after 1800 UTC (02/23). Consistent with the NARR (Figure 9), cooling begins west of ELP at this time as can be seen in the adiabatic cooling at 2100 UTC (02/23) in Table 3. By 0000–0300 UTC (02/24), the divergence tendencies, ascent, and adiabatic cooling

spread to the region surrounding the stations ELP-MAF-HOB accompanying nearly steady surface pressure and very strong forcing indicated by increasing curvature terms and  $\nabla^2\Phi$ . This is evidenced by the cooling of  $4\text{--}6^\circ\text{C}$  at 600 hPa (Figure 18 and Table 3) during the period 1800 UTC (02/23) to 0600 UTC (02/24) which results from ascent crossing over the right side of the jet exit region and ageostrophic cold-air advection near the Texas-New Mexico-Rio Grande River region (see Figure 1 for the location). By 0600 UTC (02/24), the cold pool has strengthened to  $-16^\circ\text{C}$  at 600 hPa northwest of HOB, a local cooling greater than 12 K in 12 h (Figure 18 and Table 3 at 0300 UTC), above a transition from weakly falling to rapidly rising surface pressures—where large divergence tendencies are forced by  $\nabla^2\Phi$  to support midtropospheric ascent and cooling along the path of trajectory 2.

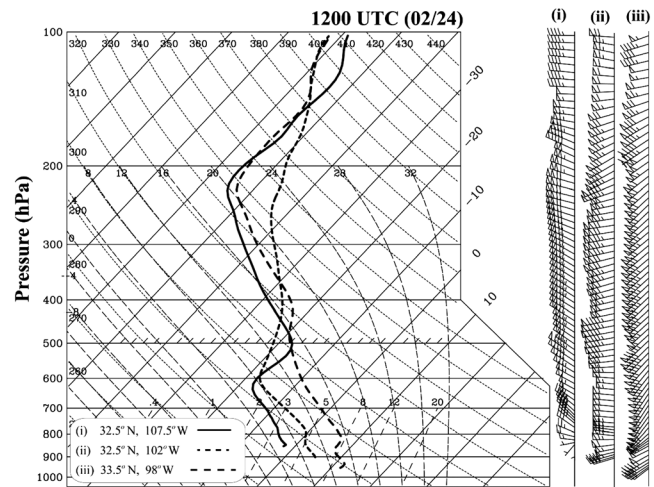


**Figure 20.** WRF (6 km grid) simulated soundings shown in skew T – ln p diagram at (i) 32.5°N, 107.5°W (solid line), (ii) 32.5°N, 102°W (short-dashed line), and (iii) 33.5°N, 98°W (long-dashed line) valid at 1200 UTC (02/24) (full barb =  $5 \text{ m s}^{-1}$ ) (see also Table 3 for the diagnosis at these locations).

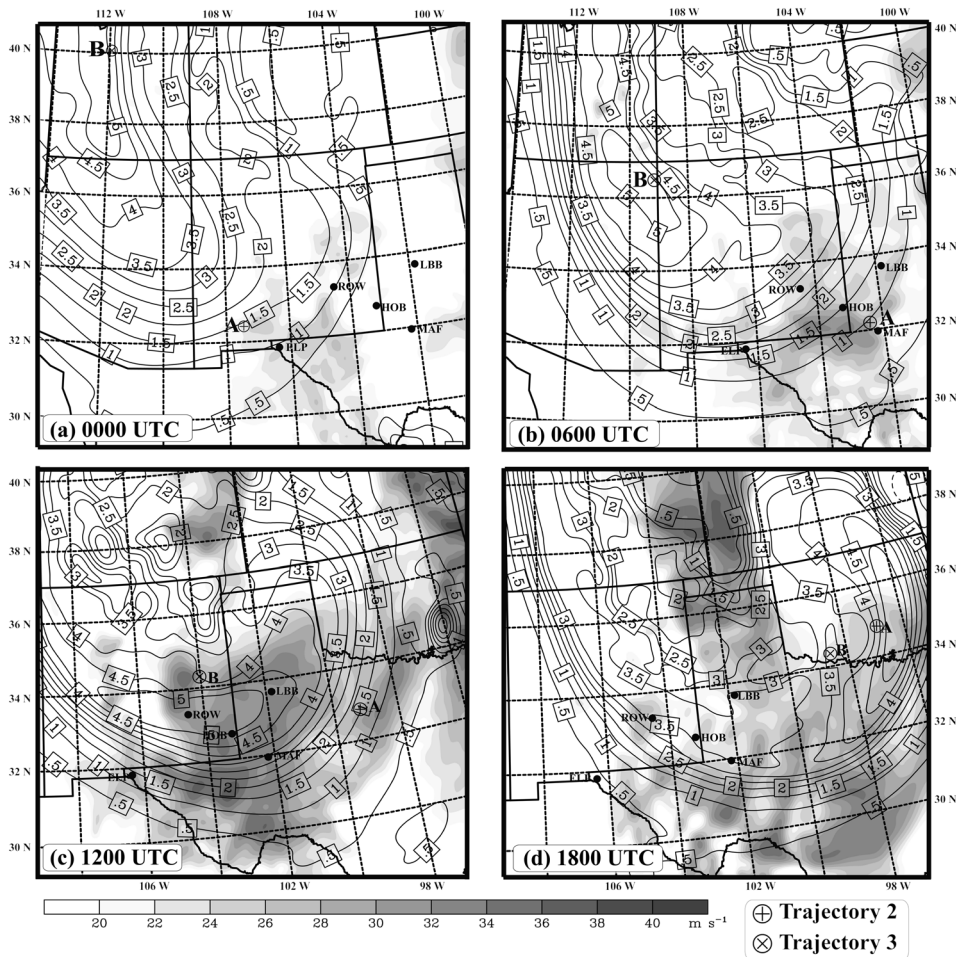


**Figure 21.** Isentropic potential vorticity (IPV) from 6 km WRF grid (contour interval=0.5 potential vorticity unit) on 310 K isentropic surface, and 800 hPa horizontal wind speeds (shaded;  $\text{m s}^{-1}$ ) valid at (a) 0000 UTC, (b) 0600 UTC, (c) 1200 UTC, and (d) 1800 UTC (02/24). Also overlain are the locations of trajectories 2 (marked at A as circled plus) and 3 (marked at B as circled times) at these times (see also Figure 14).

[35] Thus, the WRF simulation supports the sequence of increasing imbalance within the jet's exit region indicated by high Rossby numbers, ageostrophy, Lagrangian divergence tendencies, ascent, adiabatic cooling, and cold-air advection, and this sequence facilitates  $P_{\text{MSL}}$  falls early during the dust storm genesis process followed by rises as the dust storm matures and intensifies. The troughing ( $T_1$  and  $T_2$ ) and midtropospheric cooling are caused by the mass adjustments/midlevel jet accelerations after jet streak merger during the development of DS1 (during the 2100 UTC (02/23) to 0600 UTC (02/24) period). The evolution of velocity divergence in the region of large  $Ro^L$  and associated ageostrophy followed by rapid cooling (ahead of and on the warm side of the jet exit region) leads to low-level mass redistribution and generation of low-level isallobaric/ageostrophic winds [Lewis *et al.*, 2011; Kaplan *et al.*, 2011, 2013]; isallobaric/ageostrophic is simply referenced as isallobaric in the subsequent text. This linkage is further investigated by examining the  $P_{\text{MSL}}$  tendency fields in response to low-level troughing and upstream cooling aloft in the next section.

### 4.3. Mass Redistribution and Isallobaric Winds

[36] The isallobaric part ( $\vec{V}_{\text{is}}$ ) of the ageostrophic wind is given by

$$\vec{V}_{\text{is}} = -\frac{1}{\rho f^2} \nabla_z \left( \frac{\partial P_{\text{MSL}}}{\partial t} \right) \quad (3)$$

where  $\rho$  is the air density [Bluestein, 1992; Martin, 2006; Rochette and Market, 2006]. Consistent with trough development  $T_1$  through  $T_3$  as shown in Figures 10a–10c, substantial Lagrangian divergence tendencies first develop west of ELP down through MMCU at 2100 UTC (02/23) and then northeast of ELP near LBB at 0000–0300 UTC (02/24) in the high Rossby number regime. The simulated  $P_{\text{MSL}}$  falls at this location and downstream of the location are consistent with divergence aloft and mass removal from the atmospheric column. This is followed by an abrupt transition to mass accumulation before 0000 UTC (02/24) as can be inferred from the adiabatic cooling rates in excess of  $10^\circ\text{C h}^{-1}$

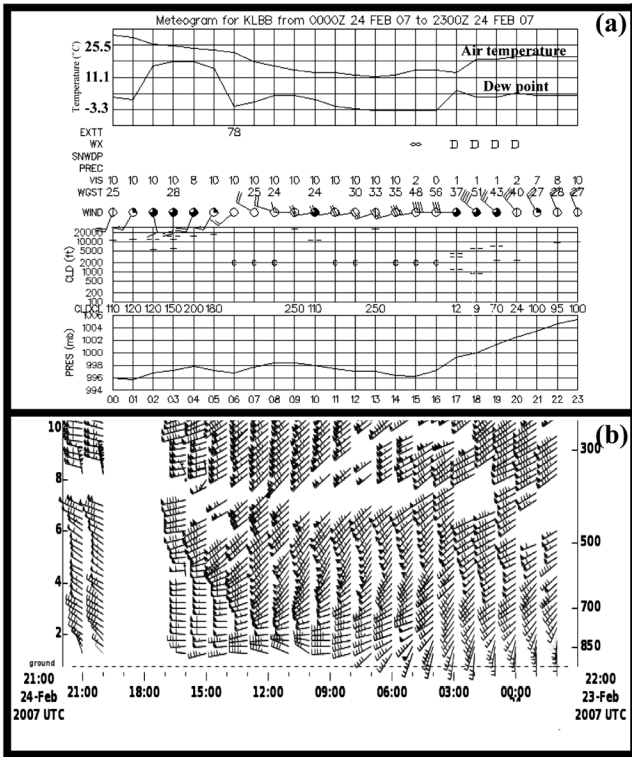


**Figure 22.** (a) Observed meteogram for Lubbock, Texas (LBB), valid from 0000 to 2300 UTC (02/24) (Source: <http://vortex.plymouth.edu>) and (b) temporal evolution of horizontal winds at Jayton, Texas (JAT; see Figure 1 for the location), from the NOAA wind profiler observations (full barb =  $5 \text{ m s}^{-1}$ ) (Source: <http://madis-data.noaa.gov>) valid from 2200 UTC (02/23) to 2100 UTC (02/24).

accompanying the upward vertical motions (Table 3). Notice that the  $P_{\text{MSL}}$  fall/rise transition results from the changing sign of velocity divergence along trajectory 2 (Table 3). The  $P_{\text{MSL}}$  falls arrive in the divergent midtropospheric motion along and on the right forward flank of the jet. The  $P_{\text{MSL}}$  falls associated with the surface troughs  $T_1$  and  $T_2$  are followed by  $P_{\text{MSL}}$  rises over west Texas before 0900 UTC (02/24).

[37] In summary, the  $P_{\text{MSL}}$  rises that create the isallobaric winds trail the Lagrangian parcel motion within the jet exit region and its midtropospheric cooling— $P_{\text{MSL}}$  falls (rises) occur due to middle-lower tropospheric cooling/transition from mass flux divergence to mass flux convergence (Figure 19). The pattern of  $P_{\text{MSL}}$  falls and rises results in a low-level isallobaric wind predominantly from the west upstream from  $T_1$  and  $T_2$  and later from the northwest upstream from  $T_3$  (Figures 11 and 19). The parcel diagnostics shown in Figure 15 dramatically show a peak in wind velocity as the parcel transitions from ascent to descent behind the pressure fall zone at the surface after 0300 UTC (02/24). The parcel is initially dominated by the divergence under the jet exit region and then sinks as the accelerating flow forces the convergent motions below 700 hPa accompanying cold-air advection under the midlevel jet core and jet entrance region. Simulated soundings shown in Figure 20 confirm these strengthening low-level winds from the west—in proximity to adiabatic layer formation from west

of ELP to central Texas—as ascent cools the column that is followed by convergence aloft during the 0600–1800 UTC (02/24) period.

#### 4.4. Isentropic Surface Perturbations and Turbulence Generation

[38] Figure 21 shows the sequence of isentropic potential vorticity (IPV) from 0000 to 1800 UTC (02/24) on the 310 K isentropic surface. The 310 K isentrope is near the top of the well-mixed PBL for DS1 as well as near the 600 hPa jet adjustments. There are two IPV maxima of significance. Of particular interest is the newly developing (secondary subsynoptic-scale) IPV maximum just before 1200 UTC (02/24) between Roswell (ROW), New Mexico, and LBB. This feature gradually elongates and eventually separates from the main IPV core over northeastern Arizona evident 6 h earlier, i.e., separated away from the upstream maximum within the large-scale trough’s cyclonic shear zone. We refer to this upstream maximum as the “QG maximum” at 0000 UTC (02/24). The secondary maximum forms in concert with the newly formed 600 hPa cold pool.

[39] The cold pool is detached from the upstream QG cold pool coincident with the middle-lower tropospheric thermal wind adjustment process just below 600 hPa over eastern New Mexico, northwest Texas, and southwestern Oklahoma during 0000–1200 UTC (02/24) (Figures 9 and 18). This subsynoptic-scale secondary IPV maximum is initiated in the region surrounding the stations ROW-ELP-MAF-LBB where middle-to-lower tropospheric accelerations become pronounced after 0000 UTC (02/24) under the midlevel jet exit region. This is consistent with the largest 600 hPa  $Ro^L$  maximum located near LBB at 0900 UTC (02/24) (Figure 16). This rapidly increasing secondary IPV maximum is indicative of static stability reduction due to changes in temperature, i.e., cooling aloft (600 hPa) associated with meso- $\beta$  scale unbalanced upward vertical motions and stretching under the jet’s exit region—indicative of vertical vorticity increase. That is, the vertical motions cause substantial static stability reduction near the large  $Ro^L$  maximum in the area bounded by stations ROW-ELP-MAF-LBB by 0900 UTC (02/24). The stabilization is above the well-mixed layer and well below the tropopause. It is on top of this stabilized layer that IPV increases (on the 310 K isentrope). The juxtaposition of three-coupled simultaneous processes at this time act to increase the IPV: (1) the vertical isentropic stretching in the lower and middle troposphere that produces cooling below the 310 K isentropic surface which in turn increases the static stability above 310 K, (2) vertical stretching that increases the vertical vorticity, and (3) the generation of TKE through destabilization of the atmosphere at low levels in proximity to the jet exit region—thus increasing the curl of the frictional force/mass within the deepening adiabatic and accelerating PBL below the 310 K isentropic surface (note soundings in Figure 20).

[40] The TKE generation is a proxy for enhanced low-level frictional stress due to accelerating boundary layer flow caused by (1) the isallobaric winds and (2) column cooling due to ascent and cold-air advection. Isallobaric motions accompanying the accelerating jet contribute to organizing this secondary IPV maximum which temporally and spatially links the dissipation of DS1 and the development of DS2 during 0600–1500 UTC (02/24). Note the dramatic shift to strong low-level westerlies at LBB (meteogram) and Jayton (JAT

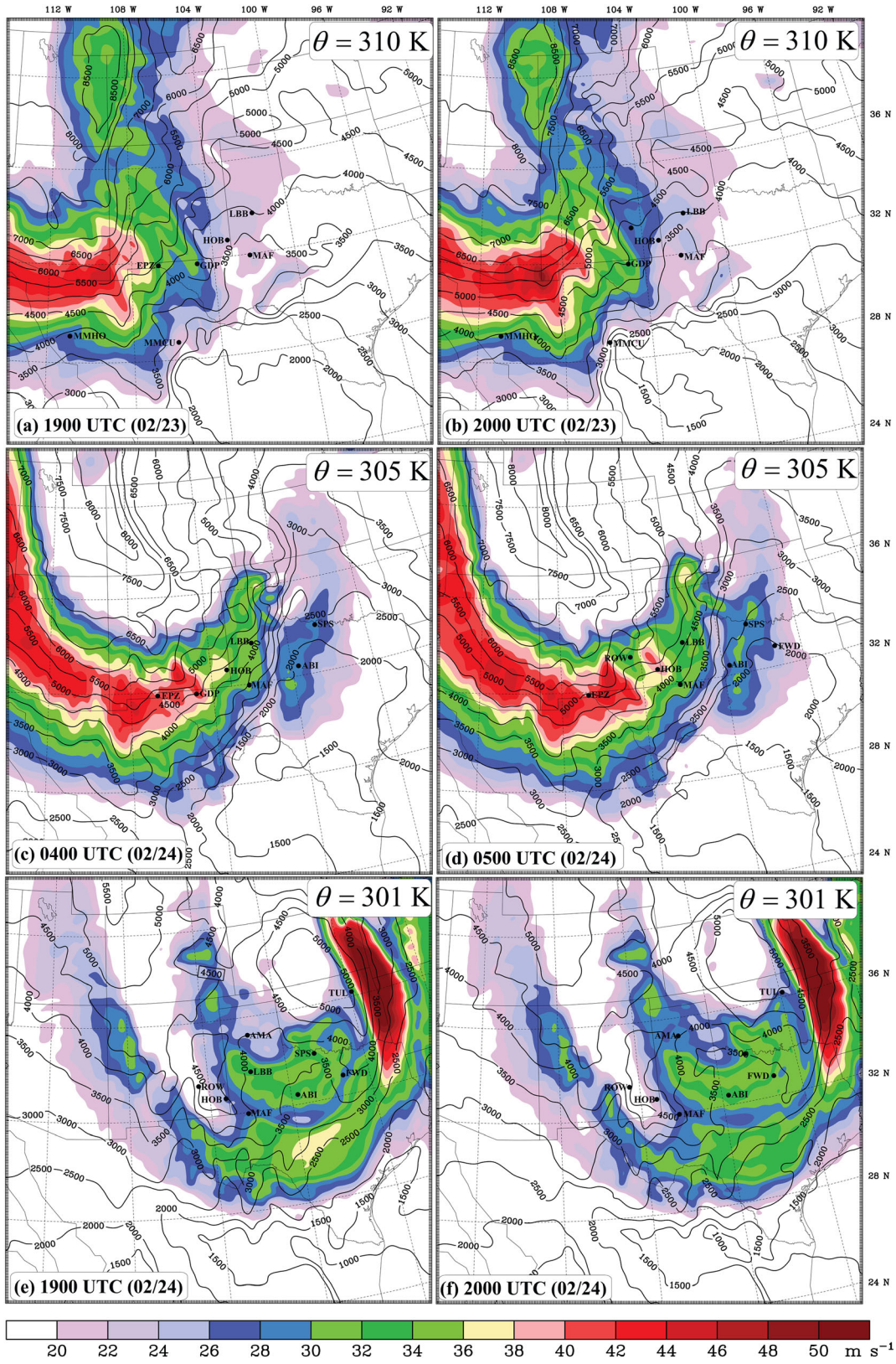


**Figure 23.** WRF (6 km grid) diagnosed horizontal winds (isotachs;  $\text{m s}^{-1}$ ) valid at (a, b) 1900 and 2000 UTC (02/23) on 310 K isentropic surface, at (c, d) 0400 and 0500 UTC (02/24) on 305 K surface, and at (e, f) 1900 and 2000 UTC (02/24) on 301 K surface. Also indicated is the height of isentropic surface (solid line; contour interval = 500 m).

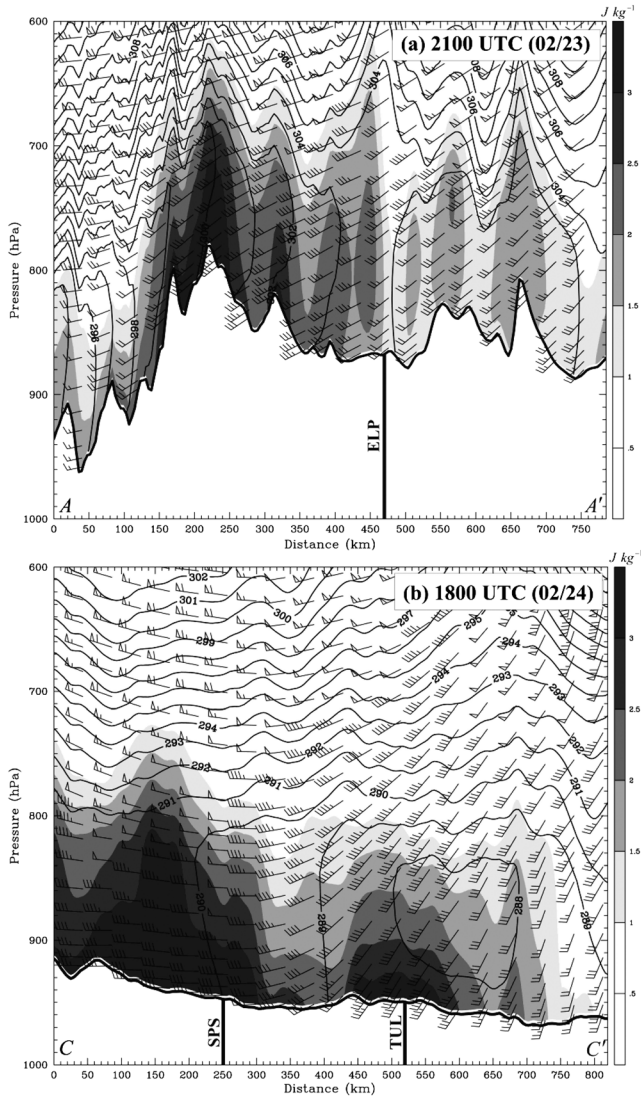


**Figure 24.** WRF (6 km grid) simulated TKE (shaded;  $J\ kg^{-1}$ ) and horizontal winds (full barb =  $5\ m\ s^{-1}$ ) and isentropes (contour interval = 1 K) along the cross sections (a) A–A’ at 2100 UTC (02/23), and (b) C–C’ at 1800 UTC (02/24) (see Figure 1 for the locations of A–A’ and C–C’). Solid black line indicates the topography. Also shown are the closest locations to ELP, SPS, and TUL along the cross sections.

profiler located near LBB) during the period 0600–1500 UTC (02/24) (Figure 22). Cold air and accelerating low-level flow create a favorable environment for low-level TKE generation particularly after sunrise in eastern New Mexico and west Texas after 1400 UTC (02/24) (0800 LST (02/24)) thus facilitating the regeneration of blowing dust at LBB, i.e., the genesis of DS2.

[41] Figure 23 shows the development of merged jet streak exit region wind maxima (or mesoscale jetlets) [e.g., Kaplan *et al.*, 1998] on the 301, 305, and 310 K isentropic surfaces. Before 1800 UTC (02/23), the 310 K surface (Figures 23a and 23b) slopes from the original QG jet front system and IPV maximum over the Utah–Nevada border southward to

northwestern Mexico as the PJ and STJ merge. During 1800 UTC (02/23) to 0000 UTC (02/24), the generation of momentum greater than  $30\ m\ s^{-1}$  on the 310 K surface builds downward to the top of the PBL ahead of the  $P_{MSL}$  rises as parcel #2 approaches the region west of ELP (see also Figures 19–24). These pressure rises are seen to develop from MMCU northwestward to southwestern New Mexico during 1800 UTC (02/23) to 2100 UTC (02/23) and then subsequently downstream between ROW and the Rio Grande River Valley during 2100 UTC (02/23) to 0000 UTC (02/24). By 2000 UTC (02/23), this process accelerates the flow within the atmospheric volume down along the 310 K surface which is also nearly coincident with the top of the deepening PBL—whose top is approximately at 650 hPa—over northeastern Mexico just southwest of EPZ and northwest of MMCU (Figures 23a and 23b).

[42] This adjustment process is also collocated with the path of parcel trajectory 2 shown in Figure 14 and the southern periphery of the newly developing 310 K IPV maximum shown in Figure 21a. Adiabatic cooling increases the PBL depth as it simultaneously expands the separation between isentropes forcing the secondary IPV feature in Figure 21 to tilt forward during confluent flow which is typical of cold frontogenesis. Note that this process is also coincident with the isallobaric flow maximum shown in Figures 19a and 19b. By 0500 UTC (02/24), the 305 K isentrope to the northeast in the region surrounding the stations HOB–LBB–MAF indicates a similar increase in predominantly ageostrophic wind flow near the top of the PBL (Figures 23c and 23d) as parcel #2 approaches west of MAF. Finally, by 1900 UTC (02/24), the region between LBB and Wichita Falls (SPS), Texas, undergoes a similar set of adjustments on the 301 K surface (Figures 23e and 23f) as parcel #2 enters eastern

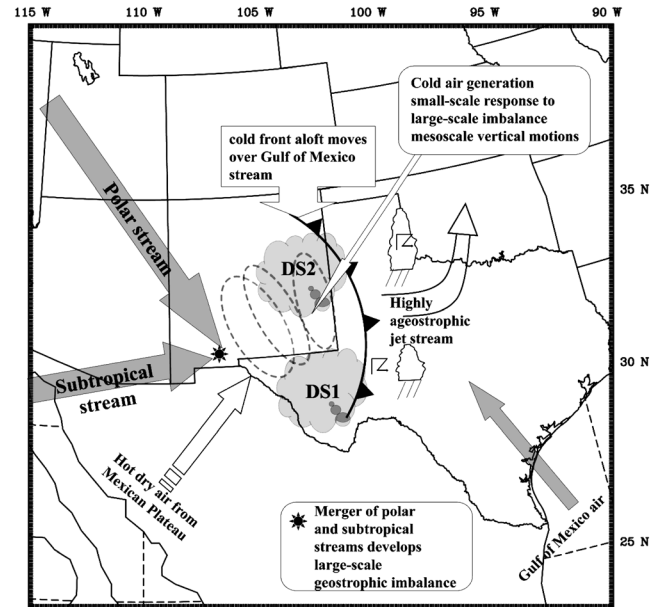


**Figure 25.** Schematic diagram of key organizing processes for the multiple dust storm events. The deep mixing in the adiabatic PBL is indicated by the dashed circles.

Oklahoma. These regions of accelerating midlevel jet exit region flow on sloping isentropic surfaces are just downstream from the soundings that indicate the expansion of dry adiabatic layers shown in Figure 20. During the period in which DS1 transitions into DS2 control of these adjustments shifts from the straight jet exit region to a more curved jet entrance region accounting for the transition from eastward to northward accelerations in the 310–301 K layer.

[43] Furthermore, the simulated momentum adjustments shown on isentropic surfaces (Figures 21 and 23) agree with the 0300–1500 UTC (02/24) wind profiler observations at JAT in the 3–7 km MSL layer and in the LBB surface meteorogram at the same time (Figure 22). Thus, the transition period between DS1 and DS2 reflects the growing accelerations and cyclonic curvature within the 310–301 K layer. The momentum adjustments link the midtroposphere to the top of the PBL. This time period marks the transition from the dominance of DS1 to DS2 as the initially straight accelerating jet exit during DS1 gives way to the curved jet entrance region during DS2. Early cooling and the increase in TKE under the merged jet streak exit region during DS1 are critical to the later period processes during DS2. This increase in TKE occurs first at 2100 UTC (02/23) (Figure 24a) within the region of the developing DS1 over northeastern Mexico, second at 0600 UTC (02/24) as DS1 extends into eastern New Mexico, and third at 1800 UTC (02/24) (Figure 24b) once DS2 is organized over northwest Texas. The deep adiabatic layers accompanying the expanding isentropic surfaces and the commensurately increasing isallobaric flow both contribute to the TKE generation and separation of the IPV maximum on 310 K (Figure 21) into two maxima, one QG upstream and highly ageostrophic downstream.

#### 4.5. Schematic Summary

[44] Figure 25 displays a broad-brush schematic of key processes that frame the mesoscale jet streak adjustments. This view involves (1) the merger of two large-scale jet streams formed in distant and different thermal regimes; (2) the development of thermal wind imbalance as cold air from the Gulf of Alaska impinges on the hot air from the elevated western plateau; (3) midtropospheric cooling due to subsynoptic ascending motions downstream from as well as on the right front flank of a developing midlevel jet streak at the merger location of the PJ and STJ, as the mass field adjusts to the wind field to ameliorate thermal wind imbalance; (4) the formation of a midtropospheric cold front and IPV maximum in response to this cooling; and finally, (5) low-level dust ablation as TKE forms in response to low-level mass adjustments, accelerating flow, and cold-air advection under the accelerating and progressively more curved jet streak.

### 5. Discussion and Concluding Remarks

[45] The differing geometries of the two successive dust storms over the Southern High Plains in late February 2007 have been investigated with a battery of tools that include surface and upper air observations, the North American Regional Reanalysis (NARR) data set, and simulations from Weather Research and Forecasting (WRF) model. The first dust storm DS1 exhibited a straight-line geometry, and the second dust storm DS2 exhibited a curved geometry. Processes on the meso- $\alpha$  and meso- $\beta$  scales of motion are central to the areas

of coverage and associated geometries of the storms. These small-scale processes occur in response to larger-scale thermal wind imbalance—an imbalance that stems from the merger of the subtropical and polar jet streams over the southwestern U.S. In this region of widespread low-bulk desert soil, the intense small-scale vertical motions create low-level instability and ageostrophic winds that ablate the dust. The study has ramifications beyond dust storm formation since it is the intense mesoscale circulation that can also lead to severe convective storm development in the presence of convective available potential energy (not widespread or substantial in this case study).

[46] The graphic that best captures the changes in the jet streaks is shown in Figure 23. Over the time period 1900 UTC (02/23) through 2000 UTC (02/24)—a time period that includes prestorm DS1 and late-storm DS2—the analyses of jet streaks on isentropic surfaces clearly show how a westerly surge of momentum associated with the straight-line dust plumes of DS1 gives way to a curved path of dust associated with DS2. Restoration of balance on the large-scale requires relative cooling on the northwest downstream side of the eastward advancing jet stream merger and coincident cross-mountain flow. This cooling occurs in part from processes identified by Danielsen—isentropic potential vorticity (IPV) transport. Yet, the scenario is more complex than highly conservative IPV evolution with a Rossby wave. It involves baroclinic subtropical-midlatitude interaction over complex terrain that modifies the IPV. The response to imbalance over this latitudinal span displays itself most convincingly on the mesoscale where complex patterns of ageostrophy lead to convergence/divergence patterns and associated vertical motions in a dry environment that produces adiabatic warming or cooling.

[47] The vertical motion and mass adjustment create instability in the lower troposphere and compensating stability at higher levels. Near-surface pressure changes in response to the mass redistribution give rise to the isallobaric winds, and turbulence kinetic energy is created in the relatively deep adiabatic/mixed layer that is in proximity to the surface. These adjustments occur under the exit region of the newly merged jet streak during DS1 and then subsequently as curved adjustments under the entrance region during DS2. By following the evolution of the mesoscale circulations, the dynamical processes associated with DS1 support the development of DS2. Results from this study illustrate the value of fine-scale numerical simulation as a means of complementing analyzed quasi-geostrophic (QG) circulation features previously studied by J. E. Martin (unpublished manuscript, 2008) and *Schultz and Meisner* [2009] for this case. A strict QG analysis fails to identify processes that pinpoint the time and placement of the dust storms. The results also have implications for studies on aerosol transport in general.

[48] Given the scale of the adjustment mechanisms prior to dust storm formation, it is entirely possible that the existing operational suite of National Centers for Environmental Prediction (NCEP) numerical models could capture these key mechanisms in this particular case study. This assumes, however, that the initial conditions in an operational environment capture the deep mass and momentum imbalance before the thermal wind adjustment occurs. As we think about the difficulty of operationally and routinely predicting dust storms—namely the necessity of capturing this aforementioned large-

scale imbalance and associated response on the mesoscale—it is also plausible that the current observation network is woefully inadequate to predict dust storm genesis on a consistent basis, i.e., in a broad cross section of case studies. The inadequacy is especially apparent on the standard National Weather Service upper air network. The satellite observations, although invaluable in depicting the areas of dust storms (during the daylight hours with visible imagery), cannot give the required vertical structure details of mass or momentum in the troposphere. Ground-based spectral instruments such as Atmospheric Emitted Radiance Interferometer have proved valuable in depicting temperature/mass structure in the lowest several kilometers of the atmosphere in clear-sky conditions [Wagner et al., 2008]. In the presence of such valuable observations, a data assimilation strategy is required that appropriately weights the background forecasts and observations to yield an improved estimate of the atmospheric state. From this improved state, predictions that are faithful to the mesoscale signatures identified in this study hold promise for locating regions of dust storm generation on a consistent basis.

## Appendix A

[49] The terms in equation (2) are given below:

$$D = \frac{1}{a \cos \varphi} \left[ \frac{\partial u}{\partial \lambda} + \frac{\partial}{\partial \varphi} (v \cos \varphi) \right] \quad (\text{A1})$$

$$\zeta = \frac{1}{a \cos \varphi} \left[ \frac{\partial v}{\partial \lambda} - \frac{\partial}{\partial \varphi} (u \cos \varphi) \right] \quad (\text{A2})$$

$$\nabla^2 \Phi = \frac{1}{a^2 \cos^2 \varphi} \left[ \frac{\partial^2 \Phi}{\partial \lambda^2} + \cos^2 \varphi \frac{\partial^2 \Phi}{\partial \varphi^2} \right] + \left( \frac{\tan \varphi}{a^2} \right) \frac{\partial \Phi}{\partial \varphi} \quad (\text{A3})$$

$$J(u, v) = \frac{1}{a^2 \cos \varphi} \left[ \frac{\partial u}{\partial \lambda} \frac{\partial v}{\partial \varphi} - \frac{\partial u}{\partial \varphi} \frac{\partial v}{\partial \lambda} \right] \quad (\text{A4})$$

$$R_\omega = -\frac{1}{a \cos \varphi} \left[ \frac{\partial \omega}{\partial \lambda} \frac{\partial u}{\partial \varphi} + \frac{\partial \omega}{\partial \varphi} \frac{\partial}{\partial \varphi} (v \cos \varphi) \right] \quad (\text{A5})$$

$$R_c = -\left( \frac{2}{a^2 \cos \varphi} \right) \frac{\partial}{\partial \varphi} \left( \frac{u^2 + v^2}{2} \sin \varphi \right) \quad (\text{A6})$$

$$\omega = \frac{dp}{dt}; \quad f = 2\Omega \sin \varphi; \quad \beta = \frac{2\Omega \cos \varphi}{a} \quad (\text{A7})$$

where  $u$  and  $v$  are zonal and meridional components of wind, respectively,  $J(u, v)$  is the Jacobian of the velocity field,  $\zeta$  is the relative vorticity,  $p$  is the air pressure,  $\omega$  is the rate of change of  $p$  following the air motion,  $\beta$  is the latitudinal variation of the Coriolis parameter  $f$ ,  $\Omega$  is the angular rotation of the Earth, and  $\varphi$  is the latitude,  $\lambda$  is the longitude,  $a$  is the radius of the Earth,  $R_\omega$  is the tilting term, and  $R_c$  is the curvature term. And  $\Phi$  is the geopotential.

[50] **Acknowledgments.** The support for this work was funded by Marc Pitchford, Director, Division of Atmospheric Sciences, Desert Research Institute, Reno, NV. Data sets used in this study have been obtained from the data servers of NOAA National Operational Model Archive and Distribution System (NOMADS), National Center for Atmospheric Research CISL Archive, and from the web portal services of the National Weather Service Southern Region Headquarters, Plymouth State Weather Center, Naval Research Laboratory, and NOAA-MADIS. We gratefully acknowledge comments from the anonymous reviewers that helped to improve the presentation.

## References

- Betts, A. K. (1986), A new convective adjustment scheme. Part I: Observational and theoretical basis, *Q. J. R. Meteorol. Soc.*, *111*, 1306–1335.
- Betts, A. K., and M. J. Miller (1986), A new convective adjustment scheme. Part II: Single column tests using GATE WAVE, BOMEX, ATEX and Arctic air-mass data sets, *Q. J. R. Meteorol. Soc.*, *112*, 693–709.
- Bluestein, H. (1992), *Synoptic-Dynamic Meteorology in Mid-Latitudes: Principles of Kinematics and Dynamics*, vol. 1, 448 pp., Oxford Univ. Press, New York.
- Carlson, T. N. (2012), *Mid-Latitude Weather Systems*, 507 pp., Penn State University Press, Pennsylvania.
- Chen, F., and J. Dudhia (2001), Coupling an advanced land surface-hydrology model with the Penn State-NCAR MM5 modeling system. Part I: Model implementation and sensitivity, *Mon. Weather Rev.*, *129*, 569–585.
- Danielsen, E. F. (1968), Stratospheric-tropospheric exchange of radioactivity, ozone, and potential vorticity, *J. Atmos. Sci.*, *25*, 502–518.
- Danielsen, E. F. (1974), The relationship between severe weather, major dust storms and rapid large-scale cyclogenesis, Part I. Subsynoptic extratropical weather systems: Observation, analysis, modeling and prediction, Notes from a Colloquium, Volume II, Seminars and Workshop, pp. 215–241, National Center for Atmospheric Research.
- Dudhia, J. (1989), Numerical study of convection observed during the Winter Monsoon Experiment using a mesoscale two-dimensional model, *J. Atmos. Sci.*, *46*, 3363–3391.
- Ek, M. B., K. E. Mitchell, Y. Lin, E. Rogers, P. Grummann, V. Koren, G. Gayno, and J. D. Tarpley (2003), Implementation of Noah land surface model advances in the National Centers for Environmental Prediction operational mesoscale Eta model, *J. Geophys. Res.*, *108*(D22), 8851, doi:10.1029/2002JD003296.
- Eliassen, A. (1962), On the vertical circulation in frontal zones, *Geophys. Publ.*, *24*, 147–160.
- Forsythe, G. E. (1945), A generalization of the thermal wind equation to arbitrary horizontal flow, *Bull. Am. Meteorol. Soc.*, *26*, 371–375.
- Janjić, Z. I. (1994), The step-mountain Eta coordinate model: Further developments of the convection, viscous sublayer, and turbulence closure schemes, *Mon. Weather Rev.*, *122*, 927–945.
- Janjić, Z. I. (2001), Nonsingular implementation of the Mellor-Yamada level 2.5 scheme in the NCEP meso model, NCEP Office Note, No. 437, 61 pp.
- Johnson, K. C. (2006), A comparison of the Navy Aerosol Analysis and Prediction System (NAAPS) to in-situ aerosol measurements in the continental U.S.: Transport vs. local production of soil dust aerosol, Master Thesis, Colorado State University, Fort Collins, Colorado.
- Kalnay, E., M. Kanamitsu, and W. E. Baker (1990), Global numerical weather prediction at the National Meteorological Center, *Bull. Am. Meteorol. Soc.*, *71*, 1410–1428.
- Kaplan, M. L., and V. M. Karyampudi (1992a), Meso- $\beta$  scale numerical simulations of terrain drag-induced along-stream circulations. I: Mid-tropospheric frontogenesis, *Meteorol. Atmos. Phys.*, *49*, 133–156.
- Kaplan, M. L., and V. M. Karyampudi (1992b), Meso- $\beta$  scale numerical simulations of terrain drag-induced along-stream circulations. II: Concentration of potential vorticity within dryline bulges, *Meteorol. Atmos. Phys.*, *49*, 157–185.
- Kaplan, M. L., S. E. Koch, Y.-L. Lin, R. P. Weglarz, and R. A. Rozumalski (1997), Numerical simulations of a gravity wave event over CCOPE. Part I: The role of geostrophic adjustment in mesoscale jetlet formation, *Mon. Weather Rev.*, *125*, 1185–1211.
- Kaplan, M. L., Y.-L. Lin, D. W. Hamilton, and R. A. Rozumalski (1998), A numerical simulation of an unbalanced jetlet and its role in the Palm Sunday 1994 tornado outbreak in Alabama and Georgia, *Mon. Weather Rev.*, *126*, 2133–2165.
- Kaplan, M. L., R. K. Vellore, J. M. Lewis, and M. Young (2011), The role of unbalanced mesoscale circulations in dust storms, *J. Geophys. Res.*, *116*, D23101, doi:10.1029/2011JD016218.
- Kaplan, M. L., R. K. Vellore, J. M. Lewis, S. J. Underwood, P. M. Pauley, J. E. Martin, and R. Krishnan (2013), Re-examination of the I-5 dust storm, *J. Geophys. Res. Atmos.*, *118*, 627–642, doi:10.1002/jgrd.50131.
- Karyampudi, V. M., M. L. Kaplan, S. E. Koch, and R. Zamora (1995a), The influence of the Rocky Mountains in the 13–14 April 1986 severe weather outbreak. I: Mesoscale lee cyclogenesis and its relationship to severe weather and dust storms, *Mon. Weather Rev.*, *123*, 1394–1422.
- Karyampudi, V. M., S. E. Koch, C. Chen, J. W. Rottman, and M. L. Kaplan (1995b), The influence of the Rocky Mountains in the 13–14 April 1986 severe weather outbreak. II: Evolution of a pre-frontal bore and its role in triggering a squall line, *Mon. Weather Rev.*, *123*, 1423–1446.
- Lewis, J. M., M. L. Kaplan, R. K. Vellore, R. M. Rabin, J. Hallett, and S. Cohn (2011), Dust storm over the Black Rock Desert: Large-scale dynamic signatures, *J. Geophys. Res.*, *116*, D06113, doi:10.1029/2010JD014784.
- Martin, J. E. (2006), *Mid-Latitude Atmospheric Dynamics: A First Course*, 324 pp., John Wiley and Sons Ltd., West Sussex, England.

- Mellor, G. L., and T. Yamada (1974), A hierarchy of turbulence closure models for planetary boundary layers, *J. Atmos. Sci.*, *31*, 1791–1806.
- Mellor, G. L., and T. Yamada (1982), Development of a turbulence closure model for geophysical fluid problems, *Rev. Geophys. Space Phys.*, *20*, 851–875.
- Mesinger, F., et al. (2006), North American Regional Reanalysis, *Bull. Am. Meteorol. Soc.*, *87*, 343–360.
- Mlawer, E. J., S. J. Taubman, P. D. Brown, M. J. Iacono, and S. A. Clough (1997), Radiative transfer for inhomogeneous atmosphere: RRTM, a validated correlated-k model for the longwave, *J. Geophys. Res.*, *102*(D14), 16,663–16,682.
- Morrison, H., G. Thompson, and V. Tatarskii (2009), Impact of cloud microphysics on the development of trailing stratiform precipitation in a simulated squall line: Comparison of one and two-moment schemes, *Mon. Weather Rev.*, *137*, 991–1006.
- Pauley, P. M., N. L. Baker, and E. H. Barker (1996), An observational study of the “Interstate 5” dust storm case study, *Bull. Am. Meteorol. Soc.*, *77*, 693–720.
- Rochette, S. M., and P. S. Market (2006), A primer on the ageostrophic wind, *Natl. Weather Dig.*, *30*, 17–28.
- Schultz, J. A., and B. N. Meisner (2009), The 24 February 2007 North Texas dust storm: An impact weather event, *Natl. Weather Dig.*, *33*, 165–184.
- Skamarock, W. C., J. B. Klemp, J. Dudhia, D. O. Gill, D. Barker, M. G. Duda, X.-Y. Huang, and W. Wang (2008), A description of the advanced research WRF version 3, NCAR/TN-475+STR, 113 pp.
- Steenburgh, W. J., J. D. Massey, and T. H. Painter (2012), Episodic dust events of Utah’s Wasatch Front and adjoining region, *J. Appl. Meteorol. Climatol.*, *51*, 1654–1669.
- Stoelinga, M. T. (2009), A users’ guide to RIP version 4: A program for visualizing mesoscale model output. (Available from: <http://www.mmm.ucar.edu/wrf/users/docs/ripug.pdf>).
- Van Tuyl, A. H., and J. A. Young (1982), Numerical simulation of nonlinear jet stream adjustment, *Mon. Wea. Rev.*, *110*, 2038–2054.
- Wagner, T. J., W. F. Feltz, and S. A. Ackerman (2008), The temporal evolution of convective indices in storm-producing environments, *Weather Forecasting*, *23*, 786–794, doi:10.1175/2008WAF2007046.1.
- Westphal, D. L. (1999), Recent dust events as simulated by NAAPS: Navy aerosol analysis and prediction system, presented at the Workshop on Mineral Dust, Boulder, 9–11 June 1999.
- Zack, J. W., and M. L. Kaplan (1987), Numerical simulations of the subsynoptic features associated with the AVE-SESAME I Case, Part I: The pre-convective environment, *Mon. Weather Rev.*, *115*, 2367–2394.
- Zhang, F., S. E. Koch, C. A. Davis, and M. L. Kaplan (2002), A survey of unbalanced flow diagnostics and their applications, *Adv. Atmos. Sci.*, *17*, 165–183.
- Zhao, T.-P., S. Ackerman, and W. Guo (2010), Dust and smoke detection for multi-channel imagers, *Remote Sens.*, *2*, 2347–2368, doi:10.3390/rs2102347.